

1 **Comparative Analysis of the Vlasiator Simulations and MMS Observations of**  
2 **Multiple X-Line Reconnection and Flux Transfer Events**

3 **M. Akhavan-Tafti**<sup>1,2</sup>, M. Palmroth<sup>3</sup>, J. A. Slavin<sup>1</sup>, M. Battarbee<sup>3</sup>, U. Ganse<sup>3</sup>, M. Grandin<sup>3</sup>, G. Le<sup>4</sup>,  
4 D. J. Gershman<sup>4</sup>, J. P. Eastwood<sup>5</sup>, J. E. Stawarz<sup>5</sup>

5  
6 <sup>1</sup> Climate and Space Sciences and Engineering, University of Michigan, Ann Arbor, MI, USA.

7 <sup>2</sup> Laboratoire de Physique des Plasmas (LPP), CNRS, École Polytechnique, Sorbonne Université,  
8 Université Paris-Saclay, Observatoire de Paris, PSL Res Université, Institut Polytechnique de  
9 Paris, Palaiseau, France

10 <sup>3</sup> Department of Physics, University of Helsinki, Helsinki, Finland.

11 <sup>4</sup> NASA Goddard Space Flight Center, Greenbelt, MD, USA.

12 <sup>5</sup> Blackett Laboratory, Imperial College, London, UK.

13  
14  
15 Corresponding author: Mojtaba Akhavan-Tafti ([akhavant@umich.edu](mailto:akhavant@umich.edu))

16  
17  
18  
19  
20  
21  
22 **This is the author manuscript accepted for publication and has undergone full peer review but**  
23 **has not been through the copyediting, typesetting, pagination and proofreading process, which**  
**may lead to differences between this version and the Version of Record. Please cite this article**  
**as doi: [10.1029/2019JA027410](https://doi.org/10.1029/2019JA027410)**

24 **Key Points**

- 25 • Anisotropic ion distributions are reported in Vlasiator simulations and MMS observations  
26 of reconnection inflow regions
- 27 • 2D simulations suggest magnetic islands grow mainly via continuous reconnection. Island  
28 coalescence, erosion & division are also present
- 29 • Based on simulation results, ion-scale FTEs are estimated to grow at  $<+0.3 R_E^2/\text{min}$ ,  
30 becoming Earth-sized  $\sim 10$  mins after initial formation

## 31 Abstract

32 The Vlasiator hybrid-Vlasov code was developed to investigate global magnetospheric dynamics  
33 at ion-kinetic scales. Here, we focus on the role of magnetic reconnection in the formation and  
34 evolution of the magnetic islands at the low-latitude magnetopause, under southward  
35 interplanetary magnetic field (IMF) conditions. The simulation results indicate that: 1) the  
36 magnetic reconnection ion kinetics, including the Earthward-pointing Larmor electric field on the  
37 magnetospheric-side of an X-point and anisotropic ion distributions, are well-captured by  
38 Vlasiator, thus enabling the study of reconnection-driven magnetic island evolution processes, 2)  
39 magnetic islands evolve due to continuous reconnection at adjacent X-points, ‘coalescence’ which  
40 refers to the merging of neighboring islands to create a larger island, ‘erosion’ during which an  
41 island loses magnetic flux due to reconnection, and ‘division’ which involves the splitting of an  
42 island into smaller islands, and 3) continuous reconnection at adjacent X-points is the dominant  
43 source of magnetic flux and plasma to the outer layers of magnetic islands resulting in cross-  
44 sectional growth rates up to  $+0.3 R_E^2/\text{min}$ . The simulation results are compared to the  
45 Magnetospheric Multiscale (MMS) measurements of a chain of ion-scale flux transfer events  
46 (FTEs) sandwiched between two dominant X-lines. The MMS measurements similarly reveal: 1)  
47 anisotropic ion populations, and 2) normalized reconnection rate  $\sim 0.18$ , in agreement with theory  
48 and the Vlasiator predictions. Based on the simulation results and the MMS measurements, it is  
49 estimated that the observed ion-scale FTEs may grow Earth-sized within  $\sim 10$  minutes, which is  
50 comparable to the average transport time for FTEs formed in the subsolar region to the high-  
51 latitude magnetopause. Future simulations shall revisit reconnection-driven island evolution  
52 processes with improved spatial resolutions.

53  
54

## 55 1. Introduction

56 Akhavan-Tafti et al. (2019) classified FTE growth mechanisms into two main categories: 1) FTE  
57 growth via adiabatic expansion due to decreasing external pressure away from the reconnection  
58 region, and 2) magnetic reconnection. In the latter category, FTE growth occurs via continuous  
59 supply of magnetic flux and plasma to the outer layers of FTEs by reconnection at adjacent X-  
60 lines and/or coalescence with the neighboring FTEs.

61

62 **Figure 1** shows a magnetic island which is a 2D projection of a flux rope generated due to primary  
63 multiple X-lines reconnection. The magnetic island can grow via continuous reconnection  
64 (Akhavan-Tafti, Slavin, Eastwood, et al., 2019) at adjacent X-lines. The X-lines at the two ends of  
65 the magnetic island are represented as ion diffusion regions (IDR). Inside IDR, inflowing ions ( $V_{in}$ ;  
66 green arrows) are demagnetized and accelerated outward as perpendicular jets (solid red arrows)  
67 and field-aligned currents (FACs; red-stroke arrows). The electron diffusion region (EDR), not  
68 shown here, is located inside the IDR (Burch et al., 2016). Electrons become demagnetized inside  
69 the EDR before becoming energized by the reconnection’s magnetic-to-kinetic energy conversion.

70

71 At the subsolar magnetopause, where FTEs are likely generated (e.g., Lee & Fu, 1985; Akhavan-  
72 Tafti et al., 2018), the magnetic field strength and plasma properties of reconnecting field lines are  
73 asymmetric across the X-line. Theory and observations have linked this asymmetry to anisotropic  
74 (i.e., non-Maxwellian) ion and electron velocity distribution functions (VDFs) in the inflow and  
75 outflow regions (e.g., Egedal et al., 2011; Hesse et al., 2014; Bessho et al., 2016; Burch et al.,  
76 2016).

77  
78 Sharp spatial gradients, sub-gyro-period temporal variations, or sources and sinks in phase space  
79 can give rise to non-gyrotropic distribution functions. Gyrotropy is a measure of a distribution  
80 function's weighted average of variances of velocities perpendicular to the local field direction  
81 (Aunai *et al.*, 2013; Swisdak, 2016; Che *et al.*, 2018). Non-gyrotropic, also known as agyrotropic,  
82 plasma populations depend on gyro-phase angle and, therefore, they are not in thermal equilibrium.  
83 They carry excess energy and may excite unstable waves (e.g., Motschmann *et al.*, 1999).  
84 Crescent-shaped VDFs are a class of non-gyrotropic plasma distributions. They are indicative of  
85 the reconnection diffusion region and are often observed in spacecraft measurements (Nagai *et al.*,  
86 2015; Burch *et al.*, 2016) and simulations (e.g., Hesse *et al.*, 2014; Bessho *et al.*, 2016).

87  
88 Magnetic islands, which are, to a first-order approximation, two-dimensional projections of flux  
89 ropes, can grow due to magnetic reconnection (e.g., Akhavan-Tafti, Slavin, Eastwood, *et al.*, 2019).  
90 Simulations and observations have also indicated that the cross section of a magnetic island can  
91 be reduced due to reconnection (e.g., Øieroset *et al.*, 2011; Hiroshi Hasegawa *et al.*, 2016). The  
92 role of reconnection in determining magnetic island dynamics can be divided into four overarching  
93 categories: 1) coalescence, 2) continuous reconnection, 3) erosion, and 4) division. **Figure 2**  
94 represents simplified schematics of the four categories. These reconnection-driven island  
95 dynamics are not necessarily independent and, thus, can take place concurrently. Individual  
96 magnetic islands are represented with concentric circles. The last reconnected-field lines are  
97 depicted with bold solid lines and the newly-reconnecting field lines, i.e., magnetic separatrix, are  
98 shown with dashed lines. The solid and hollow arrows determine the convection speed flowing  
99 into and out of the reconnection site, respectively.

100  
101 In the first category, labelled as Q1, two magnetic islands coalesce. The two neighboring islands  
102 merge and create one island whose area,  $A$ , is larger than either of the two islands. However,  
103 reconnection at the outer layers of the two merging islands will reduce the overall magnetic flux,  
104  $\psi$ . Therefore, the resulting magnetic island has a larger cross section ( $A_{product} > A_2, A_1$ ) and  
105 contains equal or greater magnetic flux ( $\psi_{product} = \psi_{larger\ island} > \psi_{smaller\ island}$  in the two-dimensional  
106 case and  $\psi_{product} > \psi_{larger\ island} > \psi_{smaller\ island}$  in three-dimensional coalescing flux ropes with a shear  
107 angle) than at least one of the two original islands (cf. Figure 1 in Akhavan-Tafti, Slavin, Eastwood,  
108 *et al.*, 2019). The second category, Q2, involves island growth due to continuous reconnection at  
109 the adjacent X-lines. Here, the continuous supply of magnetic flux to the outer layers of the  
110 magnetic island enlarges the structure, both in terms of magnetic flux and area ( $\Delta\psi > 0$  and  $\Delta A >$   
111 0).

112  
113 In the other two categories, the overall cross-sectional area of the magnetic island is reduced over  
114 time, due to magnetic reconnection. In these categories, magnetic reconnection either peels off the  
115 outer most layers of a magnetic island, called 'erosion,' Q3, or it divides a magnetic island into  
116 two smaller magnetic islands, known as 'division,' Q4 (e.g., Øieroset *et al.*, 2011; Hiroshi  
117 Hasegawa *et al.*, 2016). In both cases, the area of the original magnetic island(s) decreases with  
118 time. For instance, during the coalescence process, the smaller island will be eroded by the larger  
119 of the two merging islands. Similar processes are also reported in the magnetotail wherein an  
120 earthward-moving flux rope is eroded when interacting with the geomagnetic field (e.g., Lu *et al.*,  
121 2015; Man *et al.*, 2018; Poh *et al.*, 2019).

122

123 Theory and simulation have attempted to determine the dynamics of magnetic islands that are  
124 generated by multiple X-lines reconnection (e.g., *Daughton et al.*, 2009; *Dorelli & Bhattacharjee*,  
125 2009; *Fermo et al.*, 2010; *Uzdensky et al.*, 2010). In particular, it is essential to understand how  
126 these islands develop from birth at small spatial scales to macroscale objects. In practice,  
127 simulating long current layers inside which magnetic islands are generated has proven  
128 computationally expensive. Global fluid simulations (e.g., *Raeder*, 2006; *Dorelli & Bhattacharjee*,  
129 2009) have successfully resolved these large spatial scales. However, until recently (*Chen et al.*,  
130 2017), these simulations were not capable of capturing the small-scale physics of reconnection and  
131 island formation. Global hybrid-Vlasov simulations of the magnetopause have also demonstrated  
132 the small-scale physics of magnetic island formation and growth (e.g., *Hoilijoki et al.*, 2017;  
133 *Hoilijoki et al.*, 2019).

134  
135 In the context of FTE growth, the correlation between the observed normalized reconnection rate  
136 and the change in an FTE's magnetic flux content is essential in understanding the rate at which  
137 FTEs grow from micro-scale (*Eastwood et al.*, 2016; *Akhavan-Tafti et al.*, 2018) to macro-scale  
138 (e.g., *Walker & Russell*, 1985; *Eastwood et al.*, 2012; *Imber et al.*, 2014; *Jasinski et al.*, 2016) due  
139 to reconnection. Normalized reconnection rate is defined as the electric field pointing out of the  
140 reconnection plane that drives the reconnection normalized to the reconnecting magnetic field and  
141 the local Alfvén speed. However, the normalized reconnection rate from in-situ observations  
142 cannot determine the rate at which magnetic flux is reconnected globally. The global normalized  
143 rate of reconnection is approximately 0.1 (e.g., *Cassak et al.*, 2017) and in-situ magnetospheric  
144 observations of magnetic reconnection have reported reconnection rates up to 0.2 (e.g., *Mozer et*  
145 *al.*, 2002; *Fuselier et al.*, 2005; *Phan et al.*, 2007; *Slavin et al.*, 2009; *Chen et al.*, 2017; *Genestreti*  
146 *et al.*, 2018), consistent with theory (*Cassak & Shay*, 2007; *Liu et al.*, 2017).

147  
148 In the present study, we take advantage of the hybrid-Vlasov code Vlasiator to study the evolution  
149 of magnetic islands at the magnetopause. First, the ion kinetics inside and around two adjacent X-  
150 points are investigated. A first X-point is selected to demonstrate ion dynamics at a typical  
151 magnetopause reconnection. Another X-point is located in the vicinity and in the downstream of  
152 the first X-point and further sandwiched between two magnetic islands. Next, all magnetic islands,  
153 defined as a bundle of magnetic flux function, i.e., 'O-point,' positioned between two saddle  
154 points, i.e., 'X-points', are automatically identified with an algorithm. The identified islands are  
155 then grouped into four main quadrants based on their temporal change in enclosed magnetic flux  
156 and cross-sectional area, as discussed in **Figure 2**. The temporal evolution of magnetic islands'  
157 enclosed flux and cross sectional area is further investigated to estimate the average rate of FTE  
158 growth at the magnetopause. Lastly, the Vlasiator simulation results are compared with MMS  
159 measurements of a series of FTEs embedded in a reconnecting current sheet between two dominant  
160 X-lines at the magnetopause. It is concluded that, i) despite not resolving the ion inertial length in  
161 the magnetosheath, Vlasiator simulations capture the ion kinetics in the vicinity of X-points, thus  
162 enabling the study of reconnection-driven island evolution processes, and ii) the global  
163 magnetospheric Vlasiator simulations indicate that the recently-formed, subsolar small-scale FTEs  
164 can grow macroscale at  $<+0.3 R_E^2/\text{min}$ , while being transported to the high-latitude magnetopause  
165 (e.g., *Akhavan-Tafti et al.*, 2018).

166  
167

## 168 2. Methods

### 169 2.1. Global Hybrid-Vlasov Simulation Code Vlasiator

170 The hybrid-Vlasov code Vlasiator (<http://www.helsinki.fi/en/researchgroups/vlasiator>) has been  
171 developed to investigate global magnetospheric dynamics at ion-kinetic scales (*von Alfthan et al.*,  
172 2014; *Palmroth et al.*, 2018). Vlasiator solves the Vlasov equation, evolving ions (protons) as  
173 distribution functions in three velocity-space dimensions, tracked on a cartesian grid. Electrons are  
174 treated as a cold massless charge-neutralizing fluid, and closure is provided by the generalized  
175 Ohm's law including the Hall term. The simulation used in this study is two-dimensional in real  
176 space and three-dimensional in velocity space (*Palmroth et al.*, 2013; *Palmroth et al.*, 2017;  
177 *Hoilijoki et al.*, 2017; *Jarvinen et al.*, 2018; *Juusola, Hoilijoki, et al.*, 2018; *Juusola, Pfau-Kempf,*  
178 *et al.*, 2018; *Grandin et al.*, 2019).

179  
180 The simulation domain extends within  $-94 R_E < X < +48 R_E$  and  $-56 R_E < Z < +56 R_E$ , where  $R_E$   
181 = 6371 km is the Earth's radius. The geocentric solar ecliptic (GSE) coordinates are used in which  
182 X points sunward, Y points opposite Earth's motion about the Sun, and Z points normal to the  
183 ecliptic plane. The inner boundary with a radius of  $5 R_E$  is modelled as an ideal conducting sphere.  
184 Due to the two-dimensional nature of the simulation in the ordinary space, the dipole field is  
185 implemented as a 2-D line-dipole with a strength resulting in a realistic magnetopause standoff  
186 distance (*Daldorff et al.*, 2014). The simulation initialization process involves distributing plasma  
187 with a stationary Maxwellian distribution within the simulation domain's inner boundary. The  
188 simulation is carried out for 2150 seconds of simulation time. The analysis provided in this study  
189 only includes the final 1050 seconds of the simulation run.

190  
191 We model a steady solar wind inflow at the +x boundary, with a fast solar wind of  $\mathbf{v}$  [km/s] = -750  
192  $\hat{\mathbf{x}}$ , a density of  $n_{sw}=1 \text{ cm}^{-3}$ , a proton temperature of  $T_p = 0.5 \text{ MK}$ , and a purely southward IMF of  
193 magnitude 5 nT. The fast solar wind is intended to speed up the initialization of the simulation run.  
194 The 2D spatial grid resolution is 300 km in each direction and the 3D velocity space grid is 30  
195 km/s in each direction.

196  
197 The magnetosheath ion inertial length ( $d_i \sim 150 \text{ km}$  at the magnetopause under the stated upstream  
198 conditions) is not resolved in the Vlasiator's simulation grid (spatial grid resolution = 300 km).  
199 However, in previous Vlasiator studies, such as in the modeling of collisionless shock kinetics by  
200 *Pfau-Kempf et al.* (2018), it was confirmed that, even when drastically under-resolving ion inertial  
201 scales (spatial grid resolution  $> 8 d_i$ ), Vlasiator simulations can successfully capture ion kinetic  
202 effects. In this study, we further investigate ion kinetics in magnetopause reconnection in two-  
203 dimensional Vlasiator simulations. Previous global simulations, such as magnetohydrodynamic  
204 (MHD) with embedded particle-in-cell (PIC) simulations (*Chen et al.*, 2017), have reproduced  
205 some kinetic features associated with magnetopause reconnection.

206  
207 The Vlasiator simulations use physical scale lengths to model the Earth's magnetosphere, unlike  
208 other global simulations, where characteristic scale lengths are scaled up (e.g., *Tóth et al.*, 2017).  
209 In addition, Vlasiator simulations provide noise-free VDFs which are essential in propagating  
210 physical particle distributions in anisotropic plasma regimes, such as the magnetosheath (e.g.,  
211 *Gary et al.*, 1993). A global kinetic approach such as that of Vlasiator further avoids contamination  
212 of dynamics from MHD-kinetic boundary effects.

213

## 2.2. Observational Instrumentation:

The four identical MMS spacecraft were launched in 2015 and are designed to unravel the physics of magnetic reconnection (*Burch & Phan, 2016*). The high temporal and spatial plasma measurements (Fast Plasma Investigation (FPI); *Pollock et al., 2016*) provide three-dimensional electron and ion distributions. Plasma moments are constructed from all-sky FPI electron and ion distributions at 30 ms and 150 ms cadence, respectively. The fields instrument suites (*Torbert et al., 2016*) including the fluxgate magnetometers (FGM; *Russell et al., 2016*) and the electric dual probes (EDP) (*Ergun et al., 2016; Lindqvist et al., 2016; Torbert et al., 2016*) are used for magnetic and electric field measurements. Multi-point analysis techniques (*Harvey, 1998*) are used to determine spatial gradients in fields and plasma measurements. The spacecraft separation was, on average, 10 km for our case study (Phase 1a; *Burch, Moore, et al., 2016*).

## 226 3. Results

### 227 3.1. Hybrid-Vlasov Simulation Results

#### 228 3.1.1. Vlasiator Case Study

229 As Vlasiator simulations operate directly on a mesh-based representation of 6D phase space,  
230 velocity space plots are taken straight from the instantaneous simulation state. The VDF plots are  
231 constructed within a single simulation grid cell at each individual timestep. The VDF plots  
232 presented here show re-binned slices of velocity space in the local magnetic frames, with the local  
233 plasma bulk velocity subtracted, identical to the MMS spacecraft measurements.

234  
235 Due to the sparse velocity space representation in Vlasiator (*von Alfthan et al.*, 2014), cells with a  
236 phase space density of less than  $10^{-15} \text{ s}^3 \text{ m}^{-6}$  are dropped from the simulation, except when  
237 neighbouring denser regions are present. Dropped regions are displayed as empty areas in the VDF  
238 plots.

239  
240 **Figure 3** provides three simulation timeframes to illustrate the formation and temporal evolution  
241 of a magnetic island, defined as a bundle of magnetic flux function, i.e., ‘O-point,’ positioned  
242 between two saddle points, i.e., ‘X-points’ shown in magenta, along the northern-hemisphere  
243 magnetopause. Initially (not shown here), the last open magnetosheath field line reconnects with  
244 the last closed magnetospheric field line at X1. Shortly after at  $t=2106.0 \text{ s}$ , as shown in panel a,  
245 the newly opened field line reconnects at X2, resulting in the generation of a magnetic island  
246 (diameter  $\sim 1 R_E$ ), shown in cyan. The reconnecting field lines between the two simultaneous X-  
247 points, X2 and X3, further generates an island between them, as shown by a small O-point  
248 sandwiched between X2 and X3 in panel b. Field lines shown in green continue to reconnect at X1  
249 and X2, causing the cyan magnetic island to grow with time, panels a-c, while convecting  
250 northward along the magnetopause.

251  
252 Magnetic islands are shown to form between two X-points. The onsets of the two neighboring X-  
253 points may occur at the same time (small island in **Figure 3b**) or at different times (cyan island in  
254 **Figure 3a**). The latter was originally proposed by *Raeder* (2006) and named as the sequential  
255 multiple X-line reconnection (SMXR) model. In the case of islands generated by SMXR, the  
256 islands are embedded in field lines that are on one side connected to the magnetosphere and on the  
257 other to the magnetosheath and the solar wind. Also, as shown in **Figure 3a**, both the (cyan) island  
258 and X2 are located in the exhaust region of X1. The spatial and temporal variations between X1  
259 and X2 indicate that magnetic flux must first reconnect at X1 before re-reconnecting at X2.  
260 Therefore, X2 reconnects only the magnetic flux that has already been reconnected at X1.

261  
262 The ion VDFs and electric field signatures in the vicinity of X1 and X2 are examined along two  
263 virtual spacecraft trajectories, labelled as ‘T1’ and ‘T2’ in **Figure 4**. The panels include: a&b)  $E_x$   
264 profile (black solid curve) along virtual spacecraft T1 and T2, including the Ohm’s law  
265 components, in particular, the convection term ( $-\mathbf{v} \times \mathbf{B}$ ; red solid curve) and the Hall term ( $\mathbf{J} \times \mathbf{B}/ne$ ;  
266 blue solid curve), and 1-3) ion VDFs sliced in the  $\mathbf{V}_B - \mathbf{V}_{B \times V}$  and 4-6)  $\mathbf{V}_{B \times V} - \mathbf{V}_{B \times (B \times V)}$  planes,  
267 where  $\mathbf{V}_B$  represents the velocity along the magnetic field orientation,  $\mathbf{V}_{B \times V}$  and  $\mathbf{V}_{B \times (B \times V)}$ ,  
268 respectively, along  $(\mathbf{B} \times \mathbf{V})$  and  $\mathbf{B} \times (\mathbf{B} \times \mathbf{V})$  directions, where  $\mathbf{V}$  is the ion bulk velocity. Each ion  
269 VDF is generated at a specific  $E_x$  extrema, marked in panel a or b with a vertical green solid line.  
270 The X-point crossing is marked with a vertical magenta dashed line.

271



272 Trajectory T1 demonstrates  $E_x$  signatures that are associated with a nominal magnetosheath X-  
273 point. In particular, there exists a local minimum along  $E_x$  on the magnetospheric side of the X-  
274 point, signified by a black arrow as the ‘Larmor Peak’. *Malakit et al.* (2013) proposed the  
275 formation of a Larmor electric field, defined as an in-plane electric field in collisionless  
276 asymmetric magnetic reconnection, associated with finite Larmor radius effects. Larmor electric  
277 field is independent of the Hall electric field. As theory suggests, the Larmor electric field is  
278 situated within, the narrow blue shaded regions indicated by red arrows in **Figure 3b&c**, located  
279 in the inflow region of the dissipation region where electromagnetic energy conversion occurs  
280 (*Pritchett & Mozer, 2009*). Under close inspection, weak Earth-directed electric fields can be  
281 found intermittently along the last closed field lines, but the strongest signal is found close to X1.  
282 The ion Larmor radius in this region is on the order of  $\sim 100$  km, which again shows how Vlasiator  
283 captures kinetic physics, despite not resolving the relevant spatial scales. The ion Larmor radius  
284 increases at the magnetopause and at the X-lines ( $> 300$  km).  
285

286 Larmor electric field is proposed to exist on the magnetospheric side of a collisionless asymmetric  
287 magnetic reconnection pointing toward Earth away from the X-line, i.e.,  $E_x < 0$ . The Vlasiator  
288 simulation results indicate the presence of an Earthward electric field extremum, Larmor peak  $E_x$   
289  $\sim 0.5$  mV/m located upstream and on the magnetospheric side of X1. This value is comparable to  
290 the theoretical magnitude of the Larmor electric field is estimated to be:  $E_x \sim k_B T_i / q_i r_i = 2$  mV/m  
291 (*Malakit et al., 2013*), where  $k_B$ ,  $T_i$ ,  $q_i$ , and  $r_i$  respectively represent the Boltzmann constant and  
292 ion magnetospheric temperature, electric charge, and gyro-radius.  
293

294 On the magnetospheric side of X1, the Larmor peak is followed by a strong sun-ward Hall electric  
295 field peak, labelled in **Figure 4a** as the ‘Hall Peak’. On the magnetosheath side ( $X > 8.4 R_E$ ), the  
296 x-components of the Hall and the convection terms are uni-directional, resulting in an Earthward  
297 electric field followed by a positive peak.  
298

299 The  $\mathbf{V}_B - \mathbf{V}_{B \times V}$  VDF slice at the Larmor Peak in **Figure 4** (panel a1) shows an intense and uniform  
300 core ion population,  $\mathbf{V}_B < 250$  km/s. Panel a4 further indicates the formation of a non-gyrotropic  
301 ion population in the  $\mathbf{V}_{B \times V}$  and  $\mathbf{V}_{B \times (B \times V)}$  VDF slice. The identified non-gyrotropic ion population,  
302 indicated by a red arrow in panel a4, corresponds to the so-called perpendicular crescent-shaped  
303 ion distribution, reported in association with the local  $E_x$  minimum, i.e., Larmor electric field (e.g.,  
304 *Lapenta et al., 2017*). Closer to the X-point, where  $(E_{Hall})_x$  reaches a maximum, the perpendicular  
305 crescent-shaped distributions of the higher-energy ions,  $\mathbf{V}_{B \times V} > 250$  km/s, becomes clearer, as  
306 indicated by a red arrow in panel a5. On the magnetosheath side of X1, where  $E_x$  reaches a positive  
307 maximum, the ion VDF becomes magnetosheath-like and nearly isotropic.  
308

309 At X2, the electric field profile is more complex. X2 is located in the exhaust region of X1.  
310 Compared to X1, X2 is located between two magnetic islands. **Figure 4b** provides the  $E_x$  profile  
311 along trajectory T2. The Larmor electric field, i.e., the earthward  $E_x$ , is absent on the  
312 magnetospheric side of X2. Instead,  $E_x$  has two peaks on the magnetospheric side of X2, resulting  
313 from a strong Hall electric field component. The outer  $E_x$  peak at  $X_{GSM} \sim 7.78 R_E$ , is a result of the  
314 enhanced ion convection ( $-\mathbf{V} \times \mathbf{B}$ ; red solid curve) along the X1 separatrix, while the peak at  $X_{GSM}$   
315  $\sim 7.95 R_E$ , is supported by the Hall electric field at X2.  
316

317 The ion  $\mathbf{V}_B - \mathbf{V}_{B \times V}$  VDF slices are different between trajectories T1 and T2. The non-gyrotropic  
 318 ion population in panel a4 is absent at the outer  $E_x$  peak, in panel b4. Parallel D-shaped ion  
 319 distribution is found in panel b2 and marked by a red arrow. D-shaped ion VDFs are often observed  
 320 in the reconnection exhaust region (e.g., *Cowley, 1995; Phan et al., 2004*). The parallel D-shaped  
 321 ion distribution indicates that X2 is located within and is influenced by the outflow exhaust of X1.  
 322 Perpendicular crescent-shaped ion distributions also appear closer to the X-point, as indicated by  
 323 a red arrow in panel b5, similar to panels a5. When crossing X2, the VDFs transition from  
 324 magnetospheric-type into magnetosheath-type as suggested by the high abundance of energetic  
 325 ions,  $\mathbf{V}_{B \times V} > 500$  km/s. However, unlike the magnetosheath VDFs along trajectory T1, panels b3  
 326 and b6 show strongly anisotropic ion distributions. In particular, a non-gyrotropic ion population  
 327 is identified and marked by a red arrow in panel b6, coinciding with an enhanced anti-parallel  
 328 population of ions in panel b3.

329  
 330 The presence of magnetic islands near X2 may impact the rate at which field lines enter the  
 331 diffusion region. This can be done via: 1) building-up pressure in the reconnection exhaust, i.e.,  
 332 inside islands, and/or 2) thickening the current sheet layer within which the islands propagate. The  
 333 latter can result in increasing magnetic field tension along the highly-bent reconnecting field lines,  
 334 therefore, introducing stress against the inflow flux. **Figure 5** shows the rates of reconnection at  
 335 X1 and X2 as a function of simulation time. The same two X-points, i.e., saddle points in the  
 336 magnetic flux function, are tracked between simulation frames and their reconnection rates are  
 337 determined at each time frame, similar to *Hoilijoki et al. (2017)*. The normalized reconnection rate  
 338 here is defined as the out-of-plane electric field component,  $E_y$ , at the X-point, normalized by the  
 339 inflow plasma Alfvén speed,  $v_{Ai}$ , and magnetic field magnitude,  $B$ , given thus as,

$$\mathcal{R} = E_y^{x-point} v_{Ai}^{-1} B^{-1}$$

340  
 341  
 342  
 343 where the inflow values are gathered from the simulation just upstream of the X-point. The out-  
 344 of-plane component of the electric field,  $E_y$ , are offset ( $E_y^{x-point} = E_y + \mathbf{V}_{X-point} \times \mathbf{B}$ ) by the  
 345 convection term,  $\mathbf{E} = -\mathbf{V}_{X-point} \times \mathbf{B}$ , where  $\mathbf{V}_{X-point}$  refers to the X-point's convection speed at the  
 346 magnetopause.  $\mathbf{V}_{X-point}$  is calculated by assuming the instantaneous plasma bulk velocity to  
 347 describe the motion of the X-point in space. In order to smooth out the normalization impact of  
 348 magnetosheath fluctuations such as mirror modes, visible in  $\mathbf{B}$  and  $v_{Ai}$  signatures (not shown here),  
 349 the inflow values are averaged over 5 consecutive simulation cells in the radial direction, at least  
 350  $1 R_E$  outwards from each X-point. Consistent with the latest kinetic predictions (e.g., *Liu et al.,*  
 351 *2017*), it is discovered that normalized reconnection rate can surpass the MHD threshold  
 352 normalized reconnection rate of 0.1 (*Cassak et al., 2017*). It is further revealed that the normalized  
 353 reconnection rate at X2, which is located in the exhaust region of X1 and sandwiched between two  
 354 islands, is larger than X1. In addition, the normalized reconnection rate at X2 increases with time,  
 355 while the normalized reconnection rate slowly decreases at X1.

356  
 357

### 3.1.2. Statistical Analysis

In the previous Section, it was shown how the Vlasiator code, despite not fully resolving the ion inertial length in the magnetosheath, successfully captures key ion kinetics associated with magnetic reconnection, such as anisotropic ion distributions in the inflow and outflow regions. Thus, the Vlasiator code provides, for the first time, the opportunity to study reconnection-driven magnetic island evolution processes globally at the magnetopause. In this Section, magnetic islands near the subsolar magnetopause are identified using an automated algorithm and their temporal evolution due to reconnection are examined.

Magnetic islands within the simulation are identified by searching for maxima and saddle points of the magnetic flux function (Yeates & Hornig, 2011; Hoilijoki et al., 2017). A magnetic island is defined as encapsulated loops of magnetic field lines, identified as a local maximum of the magnetic flux function (an ‘O-point’) positioned between two saddle points (‘X-points’). In other words, we require magnetic islands to be bounded by at least two X-points (Hoilijoki et al., 2019). **Figure 6a** illustrates an example simulation timeframe of the dayside magnetosphere in which the ‘X’-points and ‘O’-points are automatically identified with an algorithm. The algorithm is also capable of determining the magnetic flux,  $\psi$ , and the cross-sectional area,  $A$ , for the magnetic islands. The algorithm can further track the merging of islands, the process known as coalescence, and can distinguish X-points within the islands. We focus on subsolar magnetic islands, tracking only those where the O-point is within polar angle,  $|\theta| < 30$  degrees from the  $X_{GSE}$ -axis.

Magnetic islands are categorized based on the relative significance of the X-points and the O-points. For each island, i.e., O-point, the two dominant X-points are defined as the two saddle points with lowest flux function value, i.e., which have reconnected the most. O-points of an island, defined as a local maximum in the magnetic flux function, are located between two dominant X-points. The dominant O-point is defined as the O-point with the highest flux function value. There may exist additional X-points between two dominant X-points indicating the presence of interior islands within the dominant structure. Similar structures have been postulated (e.g., Fermo et al., 2011) and were recently observed by MMS (e.g., Hwang et al., 2018). Additionally, the relative location of dominant O-points and X-points are tracked between simulation frames. This enabled the identification of island coalescence events in which two neighboring O-points merge to create one larger island. During this process, the innermost of three dominant X-points describing two islands becomes a non-dominant inner X-point. The coalescence process is of great practical significance, hence, it has been the subject of numerous theoretical (e.g., Pritchett & Wu, 1979), experimental (e.g., Yamada et al., 1990), and observational (e.g., Wang et al., 2016; Zhao et al., 2016; Zhou et al., 2017) studies.

**Table I** summarizes the distribution of the two-dimensional magnetic islands identified at the magnetopause. A total of 4786 magnetic islands, defined as an O-point positioned between two X-points, are independently identified in one simulation run at different locations ( $|\theta| < 30$  degrees) and different timeframes. This approach is different from Hoilijoki et al. (2019), wherein individual magnetic islands were tracked across all timeframes. The O-points are divided by the algorithm into four main categories depending on their structure and evolution: 1) ‘2 X-points’ wherein reconnection at two dominant X-points forms a magnetic island, 2) ‘>2 X-points’ in which reconnection at two dominant X-points forms an O-point inside which multiple O-points and one or more additional X-points exist, 3) ‘Coalescence’ which describes the merging of two

404 independent magnetic islands during which three dominant X-points, (associated with two  
405 category 1 islands) are reduced to two dominant X-points, and 4) ‘Division’ which describes the  
406 process through which one magnetic island is divided into two independent magnetic islands,  
407 therefore, a new dominant X-point is formed between two existing dominant X-points.. The  
408 categories 3 and 4 are subcategories of the categories 2 and 1, respectively.  
409

410 In this part of the study, we focus on the evolution of magnetic islands. In particular, we are  
411 interested in reconnection-associated processes that contribute to a change in a magnetic island’s  
412 dimensions and/or flux content between two consecutive timeframes. This is achieved by  
413 identifying all magnetic islands in a given simulation timeframe, independent of other timeframes,  
414 and tracking the identified magnetic islands in a subsequent timeframe to study the change in  
415 dimensions and/or flux content between timeframes. In practice, the evolution of an island through  
416 its lifetime can involve a multitude of the above mechanisms. However, for the purposes of this  
417 study, only the evolution processes between two consecutive timeframes are considered.  
418

419 The magnetic islands are split into four main quadrants, Q1-4, based on the temporal change in  
420 magnetic flux content,  $\Delta\psi$ , and cross-sectional area,  $\Delta A$ , as described in **Figure 2**. To achieve this,  
421 the flux content and the cross-sectional area of magnetic islands in each simulation frame are  
422 compared with the previous frame (or subsequent frame; in the case of island ‘division’). There  
423 remains a sub-population of islands whose cross-sectional area does not change between two  
424 consecutive time frames. The islands in which the magnetic flux content and/or the cross-sectional  
425 area does not change between simulation frames are separated from the four quadrants and listed  
426 in the table as ( $\Delta A = 0$  and/or  $\Delta\psi = 0$ ). Our observations include:

- 427 1. Continuous reconnection at adjacent dominant X-points supplies additional magnetic flux,  
428  $\Delta\psi > 0$ , to the outer layers of the majority of ‘uniform’ magnetic islands, defined as islands  
429 with no substructure, (Category 1, Q2 & Q4; 2193/3473 ~ 63%), and those with  
430 substructure (Category 2, Q2 & Q4; 1079/1207 ~ 89%). The sizes of these islands also  
431 increase, ( $\Delta A > 0$ ; Q1 & Q2), in nearly 55 and 77 percent of islands in Categories 1 and 2,  
432 respectively.
- 433 2. Nearly 16% of islands with substructure (Category 2) exhibit simultaneous increase of  
434 magnetic flux content and reduction of cross-sectional area,  $\Delta A < 0$  (Q4).
- 435 3. The coalescence process, Category 3, is more complex. In 41% of the cases (Q1 & Q2), it  
436 involves the growth of the total enclosed area ( $\Delta A > 0$ ,  $A_{coalescence} > A_{pre,1} & A_{pre,2}$ , where  
437  $A_{coalescence}$ ,  $A_{pre,1}$ , and  $A_{pre,2}$  represent cross sectional areas of islands after and before the  
438 coalescence process, respectively). Similarly, 36% of the islands are found to ‘erode’  
439 ( $\Delta A < 0$  &  $\Delta\psi < 0$ ; Q3) when coalescing, Category 3, with larger islands. Moreover, 23%  
440 of the islands are found to compress ( $\Delta A < 0$  &  $\Delta\psi > 0$ ; Q4) during the coalescence process.
- 441 4. Magnetic island division, Category 4, involves the splitting of one magnetic island into two  
442 smaller islands (and in one case, three islands). The likelihood of identifying island division  
443 events is nearly twice that of island coalescence events suggesting that the division of  
444 magnetic islands is more common than coalescence (e.g., Øieroset *et al.*, 2011, 2019).
- 445 5. Magnetic flux and area of dividing islands, Category 4, are found to increase  
446 ( $\Delta A > 0$  &  $\Delta\psi > 0$ ; Q2) in the majority of cases, in contrary to the proposed classification in  
447 **Figure 2**. Similarly, magnetic flux is found to increase in more than 50% of the coalescing

448 islands. Island area decreases in nearly 60% of the coalescing islands. As discussed above,  
 449 when coalescing, the minor island erodes ( $\Delta A < 0$  &  $\Delta\psi < 0$ ), contributing to the growth, in  
 450 both area and magnetic flux content, of the larger island.

451 6. Most importantly, >70% of the islands evolve due to continuous reconnection only,  
 452 Category 1, further emphasizing the significance of magnetopause reconnection with the  
 453 interplanetary magnetic field.

454  
 455 Next, the evolution of magnetic islands is investigated. First, in accordance with **Figure 2**, islands  
 456 are categorized into four quadrants, Q1-4, as shown in **Figure 6b**. The upper right corner,  
 457 of the plot ( $\Delta A > 0$  &  $\Delta\psi > 0$ ) contains islands whose relative cross-sectional area increases with  
 458 growth of relative magnetic flux content, as suggested by the linear fit shown in dashed black line,  
 459  $\Delta A/A [s^{-1}] = 2.16 (\pm \bar{\sigma}_S) \Delta\psi/\psi [s^{-1}] - 0.03 (\pm \bar{\sigma}_I)$ , where  $\pm \bar{\sigma}_S = 6.4 \times 10^{-2} s$  and  $\pm \bar{\sigma}_I = 1.9 \times 10^{-3} s^{-1}$   
 460 are the standard errors ( $\bar{\sigma} = \sigma / \sqrt{n}$ , where  $\sigma$  and  $n$  respectively represent the standard deviation and  
 461 bin population size (Akhavan-Tafti, Slavin, Eastwood, et al., 2019)) for the derived slope and  
 462 intercept values, respectively. The linear fits were found using an orthogonal distance regression  
 463 method using visible data points only. Here, the magnetic flux content and cross-sectional area are  
 464 normalized to account for variations in island physical properties associated with island size  
 465 (Akhavan-Tafti et al., 2018, 2019; Hoilijoki et al., 2019).

466  
 467 In **Figure 6c**, the relative change in the magnetic islands' magnetic flux is investigated as a  
 468 function of normalized reconnection rate,  $\mathcal{R}$ . The normalized reconnection rate is determined at  
 469 the dominant X-point, i.e., lowest magnetic flux function. We find that the majority of magnetic  
 470 islands experience normalized reconnection rates between 0.05 and 0.15 and that the average  
 471 reconnection rate is about 0.07. We also find that most coalescence events, shown in red circles,  
 472 are located within this region. At lower reconnection rates,  $\mathcal{R} < 0.05$ , magnetic flux is reduced due  
 473 to reconnection, i.e., 'erosion.' In contrast, the islands' normalized magnetic flux content,  
 474  $\Delta\psi/\Delta t > 0$ , is enhanced at higher reconnection rates,  $\mathcal{R} > 0.08$ . The linear fit, shown in black  
 475 dashed line, further indicates that, as expected, the island's magnetic flux content increases with  
 476 increasing reconnection rate,  $\Delta\psi/\Delta t [Wb/km-s] = 8.6 (\pm \bar{\sigma}_S) \mathcal{R} + 0.5 (\pm \bar{\sigma}_I)$ , where  $\bar{\sigma}_S = 3.4 \times 10^{-1}$   
 477 and  $\bar{\sigma}_I = 3.9 \times 10^{-2} Wb/km-s$ .

478  
 479 Based on the above statistics, the cross-sectional areas of subsolar islands evolve, on average, via  
 480 reconnection as:

$$481 \quad \Delta A / \Delta t \left[ \text{km}^2 / \text{s} \right] \cong A \left[ \text{km}^2 \right] (\psi \left[ \text{Wb} \right])^{-1} (2.2 (8.6 \mathcal{R} + 0.5) \pm \bar{\sigma}) \times 10^3 \text{ (Eq. 1)}$$

482 where  $A$ ,  $\psi$ , and  $\mathcal{R}$  denote respectively the FTE cross sectional area (in units of  $\text{km}^2$ ) and magnetic  
 483 flux content and the normalized reconnection rate at an adjacent X-line, assuming steady and  
 484 continuous reconnection X-line. The propagated standard error  $\bar{\sigma} = 1.5 Wb/s$ .

485  
 486 Equation 1 provides likely an *upper threshold* for the rate of change of the cross-sectional area of  
 487 subsolar magnetopause FTEs. The 2D nature of the simulation grid requires all interplanetary  
 488 magnetic flux to reconnect with the magnetosphere at the magnetopause, likely resulting in over-  
 489 estimation of the reconnected flux and, therefore, faster FTE growth.

490 The purely-southward and fast upstream IMF condition may impact the above statistics and  
491 average normalized reconnection rates. *Hoilijoki et al. (2019)* compared Vlasiator island evolution  
492 under southward IMF conditions with and without a  $B_x$ -component and found that magnetopause  
493 reconnection dynamics and island frequency and size change across the northern and southern  
494 hemispheres under different upstream IMF conditions. Therefore, future analyses shall investigate  
495 island statistics under various upstream IMF conditions to further compare with spacecraft  
496 observations (*Wang et al., 2006*).

497

Author Manuscript

## 498 3.2. MMS Case Study

### 499 3.2.1. Fields and Plasma Moments:

500 On 14 December 2015 at 0058-0100 UT, the MMS spacecraft were located downward of the  
501 subsolar magnetopause, at  $[9.8, -4.3, -0.8]$   $R_{E, GSE}$  on an outbound trajectory. The IMF remains  
502 steadily southward throughout the interval with a substantial  $y$ -component (clock angle  $\sim 45$   
503 degrees).

504  
505 In-situ magnetic and plasma measurements are shown in **Figure 7**. From top to bottom, the panels  
506 include the following parameters (at the barycenter in the GSE coordinates): a) total magnetic  
507 field, b) magnetic field components, c) ion plasma density, d) ion velocity components, e) electron  
508 velocity components, f) parallel (red solid line) and perpendicular (black solid line) current density,  
509 g) parallel (red solid line) and perpendicular (black solid line) ion temperature, h) plasma beta,  $\beta$ ,  
510 defined as the ratio of plasma thermal pressure to magnetic pressure. This magnetopause crossing  
511 is described in detail by *Hwang et al.* (2018).

512  
513 At least five localized peaks in the total magnetic field are observed, as shown in magenta bars.  
514 The peaks correspond to enhancements in  $B_y$  and a bipolar signature in the tangential component  
515 of the magnetic field (not shown here). These signatures, together with, plasma density dips (panel  
516 c), parallel current density enhancements (panel f), and localized plasma beta dips (panel h) suggest  
517 the presence of  $d_i$ -scale FTE-type flux ropes (*Eastwood et al.*, 2016; *Akhavan-Tafti et al.*, 2018;  
518 *Akhavan-Tafti, Slavin, Eastwood, et al.*, 2019). *Hwang et al.* (2018) stated that the observed FTEs  
519 have diameters ranging between,  $2.5 < \lambda [d_i] < 6.8$ , where  $\lambda$  and  $d_i$  ( $= 75$  km) denote the FTE  
520 diameter and the local ion inertial length, respectively.

521  
522 The localized dips in magnetic field total coincide with ion flow enhancements and localized field-  
523 aligned current density peaks, suggesting possible reconnection in and outflow region encounters.  
524 *Hwang et al.* (2018) investigated the possible ion jets using the Walén relations (e.g., *Sonnerup et*  
525 *al.*, 1981) and concluded that the MMS spacecraft may have traversed near multiple active X-lines.  
526 They then proposed a magnetic field topology involving multiple ion-scale FTEs sandwiched  
527 between two active X-lines. **Figure 8** provides a schematic illustration of the proposed field  
528 geometry. Here, the MMS spacecraft are shown to traverse across a reconnecting magnetopause  
529 current sheet within which multiple FTEs are detected.

### 532 3.2.2. Ion Velocity Distribution Functions:

533 **Figure 8** illustrates the approximate locations and geometry of the observed ion-scale FTEs and  
534 the possible X-lines. The orientation of the FTEs (and the orientation of X-lines) is along the  
535 intermediate eigen vector ( $\mathbf{M}$ ) derived from applying the minimum variance analysis (MVA) on  
536 the magnetopause crossing. The eigen vectors (in the GSM coordinates) include:  $\mathbf{N} = [0.84, -0.36,$   
537  $-0.41]$ ,  $\mathbf{M} = [-0.46, -0.87, -0.17]$ , and  $\mathbf{L} = [0.30, -0.33, 0.89]$ . We further investigate the MMS  
538 observations of ion VDFs in the vicinity of two independent X-lines. The VDFs are particle  
539 distribution slices in the parallel and perpendicular planes.

540  
541 In **Figure 8**, the ion VDFs at the X-lines are displayed in the ion bulk velocity frame of reference.  
542 To achieve this, the components of the bulk ion velocity,  $\mathbf{v}_i$ , are subtracted from velocity  
543 distribution components. Panels 1-4 show VDF slices in the  $\mathbf{V}_B - \mathbf{V}_{B \times V}$  plane and panels 5-8

544 represent the  $\mathbf{V}_{B \times V} - \mathbf{V}_{B \times (B \times V)}$  plane, where  $\mathbf{V}_B$  represents the velocity along the magnetic field  
545 orientation, and  $\mathbf{V}_{B \times V}$  and  $\mathbf{V}_{B \times (B \times V)}$ , respectively, along the  $(\mathbf{B} \times \mathbf{V})$  and  $\mathbf{B} \times (\mathbf{B} \times \mathbf{V})$  directions,  
546 where  $\mathbf{V}$  is the ion bulk velocity. The VDF slices are also organized on the basis of ion energy  
547 range. From left to right, the panels represent ion measurements: panels 1&5) all energy bins (1  
548 eV – 30 keV), 2&6) low-energy ions (1 eV – 3 keV), 3&7) mid-energy ions (3 – 6 keV), and 4&8)  
549 high-energy ions (6 – 30 keV).

550  
551 In the vicinity of a first possible X-line encounter, panel B at the bottom of the figure, marked by  
552 a blue arrow, in the  $\mathbf{V}_B - \mathbf{V}_{B \times V}$  slice for low-energy ions (1 eV – 3 keV), there exists a non-isotropic  
553 population of ions moving anti-parallel to  $\mathbf{B}$ . The low-energy ion population,  $1 \text{ eV} < E_i < 3 \text{ keV}$ ,  
554 is gyrotropic in the  $\mathbf{V}_{B \times V}$  and  $\mathbf{V}_{B \times (B \times V)}$  slice. However, there exists a non-gyrotropic mid-energy  
555 ion population,  $3 < E_i [\text{keV}] < 6$ , with a clear shift in negative  $\mathbf{V}_B$  direction in the  $\mathbf{V}_B - \mathbf{V}_{B \times V}$  plane,  
556 i.e., parallel crescent-shaped population (e.g., *Hesse et al.*, 2014; *Wang et al.*, 2016). The high-  
557 energy ion population,  $6 < E_i [\text{keV}] < 30$ , appears sparse and likely inconclusive. The counting  
558 statistics for the  $1 \text{ eV} < E_i < 6 \text{ keV}$  ions further verified (not shown here) that the observed non-  
559 isotropic signatures are statistically significant ( $> 4$  counts per energy-angle bin). The  $6 < E_i [\text{keV}]$   
560  $< 30$  ion measurements suffer from low-counting statistics and are, thus, inconclusive.

561  
562 At a second possible X-line, marked by a red arrow in panel A at the top of the figure, the low-  
563 energy ions population is found to be symmetric in the  $\mathbf{V}_B - \mathbf{V}_{B \times V}$  plane, but non-gyrotropic, in the  
564  $\mathbf{V}_{B \times V} - \mathbf{V}_{B \times (B \times V)}$  plane. The mid-energy ions,  $3 < E_i [\text{keV}] < 6$ , show an isotropic distribution in  
565 the  $\mathbf{V}_B - \mathbf{V}_{B \times V}$  plane. However, in the  $\mathbf{V}_{B \times V} - \mathbf{V}_{B \times (B \times V)}$  plane, the ions form a non-gyrotropic,  
566 *perpendicular* crescent-shaped distribution. The high-energy ion population,  $6 < E_i [\text{keV}] < 30$ ,  
567 remains sparse and likely inconclusive. The counting statistics for the  $1 \text{ eV} < E_i < 6 \text{ keV}$  ions  
568 further verified (not shown here) that the observed non-isotropic signatures are statistically  
569 significant ( $> 4$  counts per energy-angle bin). The  $6 < E_i [\text{keV}] < 30$  ion measurements suffer from  
570 low-counting statistics and are, thus, inconclusive.

571  
572 The MMS observations further confirm the presence of ion crescent-shaped distributions in the  
573 magnetospheric side of the X-point, as shown by the Vlasiator simulations. In particular, the  
574 perpendicular crescent-shaped distribution of ions on the magnetospheric side of a Vlasiator X-  
575 point, as shown in panels a4, a5 and b5 in **Figure 4**, correspond to the MMS-observed parallel  
576 crescent-shaped mid-energy ion distribution, as shown in **Figure 8** in panel B3 & B7. The different  
577 orientation between the simulated and observed crescent-shaped distributions may be a result of  
578 2D ordinary-space simulation grid. In particular, the ratio of the out-of-plane to in-plane  
579 components of the simulated convection electric field,  $E \sim (\mathbf{B} \times \mathbf{V})$ , at the magnetopause may  
580 influence the orientation of the crescent-shaped distributions. This will be further examined in  
581 future Vlasiator simulations with 3D ordinary- and velocity-space grids.

582  
583 Similarly, MMS measurements on the magnetosheath side of a possible X-line encounter further  
584 suggest the presence of a perpendicular crescent-shaped distribution of mid-energy ions, panels  
585 A3 and A7 in **Figure 8**. The Vlasiator simulations also show the formation of a non-gyrotropic  
586 sub-population of magnetosheath ions in the  $\mathbf{V}_{B \times V} - \mathbf{V}_{B \times (B \times V)}$  plane, as indicated by a red arrow in  
587 **Figure 4** in panel b6. These finding also agrees with PIC simulations of asymmetric reconnection  
588 (*Hesse et al.*, 2014) and MMS observations (e.g., *Wang et al.*, 2016). Previously, global 3D MHD



589 with embedded PIC model simulation (MHD-EPIC) of the Earth's dayside reconnection by *Chen*  
590 *et al.* (2017) showed similar results.  
591  
592

## 593 4. Discussion

594 The main objective of this study is to provide a global perspective on reconnection-driven  
595 mechanisms through which FTEs evolve by utilizing the global Vlasiator simulations and in-situ  
596 MMS observations. It is, however, important to keep in mind the two major differences between  
597 MMS observations and Vlasiator simulations:

- 598 1. The upstream solar wind conditions and the spacecraft location at the time of the encounter  
599 are somewhat different between in-situ observations and the Vlasiator simulations results.  
600 In particular, our simulated upstream solar wind conditions lack the IMF  $B_y$  (out-of-plane)  
601 and IMF  $B_x$  (Hoilijoki *et al.*, 2019) components. The former component is an essential  
602 contributor to the formation of 3D flux ropes' core field (e.g., Daughton *et al.*, 2011).
- 603 2. The two-dimensional simulations generate magnetic islands whose central region are  
604 characterized by high density (Markidis *et al.*, 2013) and low magnetic field magnitude,  
605 contrary to the observed profiles inside flux ropes (Akhavan-Tafti, Slavin, Eastwood, *et*  
606 *al.*, 2019). In fact, magnetic islands collect much of the outflow plasma from adjacent  
607 reconnection X-points. In three dimensions, the outflowing plasma in an X-line's exhaust  
608 region can flow along the out-of-plane component of the magnetic field at the outer layers  
609 of flux ropes (Ma *et al.*, 1994; Zhang *et al.*, 2010; Chen *et al.*, 2017). Future Vlasiator  
610 simulations will further investigate the three-dimensional aspects of FTEs at the  
611 magnetopause.

### 612 4.1. Reconnection Signatures

613 The first step in studying reconnection-driven processes at the magnetopause was to confirm that  
614 reconnection signatures were captured by the hybrid-Vlasov Vlasiator simulations. We find that,  
615 despite the Vlasiator simulations not fully resolving the ion inertial length in the magnetosheath,  
616 the Vlasiator 2D simulations and the MMS observations agree in some important and critical  
617 aspects, including:  
618

- 619 1. FTE generation via multiple X-line reconnection: The cyan Vlasiator magnetic island  
620 depicted in **Figure 3a** is generated between two adjacent X-points. The formation  
621 mechanism for the two X-points is sequential in nature, similar to the sequential multiple  
622 X-line reconnection (SMXR) model proposed by Raeder (2006) under southward IMF  
623 conditions. The SMXR model suggests that an initial X-line reconnects field lines. A  
624 second X-line is then formed in the vicinity of the first X-line, resulting in the formation  
625 of an FTE.

626 Spacecraft observations (e.g., Trattner *et al.*, 2012) have provided evidence for the multiple  
627 X-line reconnection model by Lee & Fu (1985). For instance, Fear *et al.* (2008) used  
628 Cluster observations to show that the azimuthal extension of an observed FTE could not  
629 be explained by the elbow-shaped FTE model. THEMIS observations have similarly found  
630 bi-directional electron flows inside FTEs further suggesting the need for a second X-line  
631 to close the field lines (Hasegawa *et al.*, 2010). Recently, MMS observations provided  
632 further evidence for multiple X-line reconnection at the magnetopause. In particular,  
633 Fuselier *et al.* (2018) showed the presence of adjacent X-lines at the magnetopause under  
634 southward IMF conditions, i.e., large IMF clock angles, similar to our simulations'  
635 upstream conditions.

636 Multiple localized total magnetic field extrema are observed in the in-situ magnetic field  
637 measurements, as indicated in **Figure 7**. Further investigation of plasma measurements  
638 suggests that  $|B|$ -peaks are ion-scale FTEs dispersed within a thin reconnection current  
639 sheet, as indicated by the ion jet reversals satisfying the Walén relations (see *Hwang et al.*,  
640 2018) and current density enhancements. The FTEs are likely generated via multiple X-  
641 line reconnection and the associated tearing-mode instability (e.g., *Lee & Fu*, 1985;  
642 *Akhavan-Tafti et al.*, 2018; *Fuselier et al.*, 2018; *Hwang et al.*, 2018). In the proposed  
643 topology, in agreement with the SMXR model and the Vlasiator simulation results, a  
644 second X-line causes the generation of FTEs.

645 Vlasiator simulations further indicate that the reconnection rate can vary between adjacent  
646 X-points. As shown in **Figure 5**, the reconnection rate at X2 in **Figure 3a**, located in the  
647 exhaust region of X1, increases with time while the reconnection rate at the Southern X-  
648 point is reduced. This may be due to the reconnection exhaust geometry. X2 is sandwiched  
649 between two magnetic islands of different scales, while X1 is surrounded by one island and  
650 a semi-infinite current sheet. This finding may further underpin the significant role of flux  
651 ropes in reconnection dynamics by unblocking the exhaust region and providing a path  
652 along which the outflowing plasma can efficiently propagate.

- 653 2. Larmor electric field: The Larmor electric field is proposed to exist on the magnetospheric  
654 side of a collisionless asymmetric reconnection site, and should be pointing toward Earth  
655 away from the X-line,  $E_x < 0$  (*Malakit et al.*, 2013). The Vlasiator simulation results indicate  
656 the presence of an Earthward electric field extremum, Larmor peak  $E_x \sim 0.5$  mV/m located  
657 upstream and on the magnetospheric side of X1, in **Figure 3b&c**. This value is comparable  
658 to the theoretically-estimated magnitude:  $E_x \sim 2$  mV/m. The global 3D MHD-EPIC  
659 simulation of the Earth's dayside reconnection by *Chen et al.* (2017) showed similar  
660 localized Earthward-pointing electric fields that precede a strong sunward electric field.
- 661 3. Anisotropic ion distributions in the vicinity of a reconnection site: The Vlasiator  
662 simulations indicate the formation of a perpendicular crescent-shaped distribution of ions  
663 in the magnetospheric inflow region of the X-points, sometimes associated with the Larmor  
664 electric field, such as in Figure 4 panel a4 (e.g., *Lapenta et al.*, 2017). The crescent-shaped  
665 ion population becomes clearer closer to the X-point, as shown in **Figure 4** panel a5. Non-  
666 gyrotopic, crescent-shaped ions are also observed during possible reconnection inflow  
667 region encounters, as shown in panels A7 and B3 in **Figure 8**. Further investigation is  
668 needed to examine and compare the observed and simulated non-isotropic ion distributions  
669 in the magnetosheath as well as the magnetospheric reconnection inflow regions.  
670 Furthermore, the roles of upstream solar wind conditions, local energization mechanisms  
671 (*Akhavan-Tafti, Slavin, Sun, et al.*, 2019), and the magnetopause convection electric field  
672 orientation in determining the properties of anisotropic ion distributions in reconnection  
673 inflow regions shall be investigated.

674 Future investigations will use 3D spatial and velocity simulations under more representative  
675 upstream conditions to improve the above results.

## 676 4.2. Magnetic Island Evolution

677 After confirming that the Vlasiator simulations captured key reconnection signatures, the next step  
678 was to determine the relative roles of the different reconnection-driven mechanisms through which  
679 magnetic islands evolve, as described by the introductory **Figure 2**. A total of 4786 subsolar  
680 islands ( $|\theta| < 30$  degrees) are identified across time frames. The islands are divided into four main  
681 categories depending on their structure and evolution: 1) '2 X-points', 2) '>2 X-points', 3)  
682 'Coalescence,' and 4) 'Division.' It is concluded that:

- 683 1. On average, continuous reconnection at adjacent dominant X-points supplies additional  
684 magnetic flux,  $\Delta\psi > 0$ , to the outer layers of magnetic islands. The additional supply of  
685 magnetic flux further causes an increase ( $\Delta A > 0$ ) in the cross-sectional areas of the  
686 majority of these islands, as proposed by *Akhavan-Tafti et al.* (2019; cf. Figure 1).
- 687 2. In 16% of the islands belonging to Category 2, magnetic flux content increases while the  
688 islands' cross-sectional area is reduced, Q4. This suggests that the internal X-points may  
689 contribute to dividing the dominant island into at least two smaller islands, i.e., island  
690 division. Another possible scenario, as postulated by *Akhavan-Tafti et al.* (2019), may  
691 include the compression of the island due to the radially-inward force from the continuous  
692 supply of magnetic flux at adjacent X-points ( $\Delta A < 0$  &  $\Delta\psi > 0$ ), before the island grows in  
693 dimensions.
- 694 3. In the Coalescence category, 42% of the magnetic islands grow in dimensions (Q1 and Q2)  
695 while 42% are eroded, i.e., reduction in cross-sectional area (Q1 and Q3). These suggest  
696 that, as discussed by *Fermo et al.* (2011), the coalescence process involves the merging of  
697 two neighboring islands wherein the smaller of two islands is consumed, i.e., eroded  
698 ( $\Delta\psi < 0$ ), by the larger island.
- 699 4. The likelihood of identifying island division events is nearly twice that of island  
700 coalescence events suggesting that the division of magnetic islands is more common than  
701 coalescence (e.g., *Øieroset et al.*, 2011, 2019), at least in two-dimensions. While  
702 identifying the two processes in spacecraft observations is challenging, one approach in  
703 distinguishing flux rope coalescence from division is to investigate the relative structure  
704 velocities. In the coalescence process, the two neighboring flux ropes approach each other  
705 (in the flux ropes' frame of reference), whereas in the division process the structure velocity  
706 vectors point in opposite directions (moving away from one another).
- 707 5. The proposed classification in **Figure 2** oversimplifies the island dynamics by neglecting  
708 the fact that one or two of the processes could occur concurrently. For instance, in Category  
709 3, the two X-points on the outer edges of the two coalescing islands can and do continue  
710 to supply additional magnetic flux and plasma to the outer layers of the two islands.
- 711 6. Continuous reconnection, Category 1, is the dominant contributor to island evolution (e.g.,  
712 *Paschmann et al.*, 1982; *Akhavan-Tafti, Slavin, Eastwood, et al.*, 2019). However, this  
713 result may also be due to the 2D nature of our simulations and/or our island selection  
714 criteria wherein islands are defined as 'O-points' sandwiched between two 'X-points.'

715 Future 3D spatial and velocity simulations will re-examine the relative roles of the reconnection-  
716 driven FTE evolution mechanisms.

### 4.3. FTE Growth Rate

Finally, the Vlasiator simulations' global perspective on the evolution of magnetic islands via reconnection-driven mechanisms can be further utilized to inform in-situ observations. In particular, spacecraft observations are not capable of studying the temporal evolution of individual FTEs. Therefore, global simulations can further be used to interpret spacecraft observations. In this Section, the normalized reconnection rate as measured by the MMS spacecraft in the vicinity of a possible reconnection inflow region located between two ion-scale FTEs is used in combination with the Vlasiator island statistics in order to estimate the rate at which the two FTEs may grow via reconnection.

The Vlasiator simulations indicate that the change in magnetic island magnetic flux content,  $\Delta\psi$ , due to continuous reconnection at adjacent X-lines is a function of normalized reconnection rate. In 2D, the magnetic flux content is described as the enclosed in-plane flux within an area and, therefore, it is, in practice, different from in-situ observations. However, the rate of change in magnetic flux,  $\Delta\psi$  [Wb/s-km], is, to a first-order approximation, similar in 2D simulation results and spacecraft observations. The rate of change in magnetic flux is determined in the reconnection plane (per X-line length) along the X-line.

*Hoilijoki et al. (2019)* confirmed that the size distribution of Vlasiator magnetic islands at the magnetopause is similar to that of the subsolar FTEs as observed by MMS and reported by *Akhavan-Tafti et al. (2018)*. Here, we determine the reconnection rate  $\mathcal{R}$  of a possible X-line positioned near an observed  $d_i$ -scale FTE to estimate the FTE's rate of growth based on the Vlasiator simulation island statistics (Equation 1 in Section 3.1.2).

**Figure 9** shows the observed FGM magnetic field vectors, the bulk FPI ion and electron velocities and the EDP electric field vectors at the location of MMS1 in the vicinity of a possible X-line encounter sandwiched between two of the observed FTEs, marked with a cyan bar in **Figure 7**. The vectors are transformed into the LMN coordinate system where the LMN eigen vectors (in the GSM coordinates) are:  $\mathbf{N} = [0.84, -0.36, -0.41]$ ,  $\mathbf{M} = [-0.46, -0.87, -0.17]$ , and  $\mathbf{L} = [0.30, -0.33, 0.89]$  (*Hwang et al., 2018*). High-resolution electric field measurements are boxcar-averaged to match the cadence of the FPI electron measurements, i.e., 30 ms. Using MVA and the timing analysis techniques, the X-line is found to convect at a normal velocity  $\mathbf{v}_{structure}$  [km/s] =  $130 * [-0.96, 0.29, 0.06]$  LMN, as reported by *Hwang et al. (2018)*. Therefore, the electric field vector in the X-line's frame of reference can be estimated as  $\mathbf{E}_{X-line} = \mathbf{E} + \mathbf{v}_{X-line} \times \mathbf{B}$  (panel f).

The observed MMS estimated out-of-plane component of electric field,  $E_M$ , averaged at the vicinity of the X-line within the purple-shaded interval is  $E_{M, obsv} = 0.2$  mV/m. This corresponds to an averaged normalized reconnection rate,  $\mathcal{R} = E_M / V_{Ai} B_{MSH} = 0.18$ , where  $V_{Ai}$  and  $B_{MSH}$  are the average upstream Alfvén velocity (panel g) and magnetic field magnitude (panel a), respectively (e.g., *Liu et al., 2017; Genestreti et al., 2018*). Based on the Vlasiator simulation fit of  $\Delta\psi/\Delta t$  [Wb/km-s] =  $8.6 \mathcal{R} + 0.5$ , where  $\mathcal{R}$  represents the rate of reconnection, it is concluded that, to a first-order approximation, the observed  $d_i$ -scale FTE ( $\psi = 4.4$  kWb) can gain magnetic flux at rate  $< +9.0$  kWb/s-km due to continuous supply of magnetic flux at the adjacent X-lines. At this rate, this FTE will contain 1 MWb of magnetic flux (e.g., *Wang et al., 2005*) in nearly 2 minutes.

763 The global Vlasiator simulations results are further utilized to determine the average rate at which  
764 FTEs grow ( $\Delta A/\Delta t$ ) at the magnetopause. From the MMS-observed normalized rate of  
765 reconnection rate,  $\mathcal{R} = 0.18$ , and ion-scale FTE sizes and magnetic flux contents, it is determined  
766 that the ion-scale FTE observed in the vicinity of an X-line may grow in size at rate:

$$767 \quad \Delta A/\Delta t (\lambda=6.8 d_i, \mathcal{R}=0.18, \psi=4.4 \text{ kWb}) \leq +2.1(\pm 0.7) \times 10^5 \text{ [km}^2/\text{s]} = +3.1(\pm 0.1) \times 10^{-1} \text{ [R}_E^2/\text{min}].$$

768 At this growth rate, the ion-scale FTE will grow Earth-sized,  $r = 1 R_E$  (e.g., *Eastwood et al.*, 2012),  
769 in  $10.2^{+5}$  minutes due to steady and continuous reconnection at adjacent X-lines while convecting  
770 away from the subsolar region along the magnetopause. This estimated growth duration is  
771 comparable to the transport time for an FTE forming at the subsolar magnetopause to reach the  
772 high-latitude magnetopause, i.e.,  $\sim 10$  minutes (e.g., *Owen et al.*, 2001). Future studies will focus  
773 on the evolutions of ion-scale (e.g., *Sun et al.*, 2019) and large-scale flux ropes (e.g., *Slavin et al.*,  
774 1995; *Slavin, et al.*, 2003) in the Earth's magnetotail.

775  
776 As noted previously, the above-estimated FTE growth rate is likely an *upper threshold* for the rate  
777 of change of the cross-sectional area of subsolar magnetopause FTEs. The 2D nature of the  
778 simulation grid requires all interplanetary magnetic flux to reconnect with the magnetosphere at  
779 the magnetopause, probably resulting in over-estimation of the reconnected flux and, therefore,  
780 faster FTE growth. Additionally, accurate determination of the reconnection plane orientation is  
781 key for measuring reconnection rate (e.g., *Genestreti et al.*, 2018). In this study, the MVA  
782 technique is used to determine the reconnection plane. As provided in the Supplemental Table S1,  
783 we rely on the fact that the applications of MVA on magnetic field (MVA B) and electron velocity  
784 (MVA Ve) measurements for the this partial magnetopause crossing generate similar intermediate  
785 ( $\hat{M}$ ) eigen vectors. However, there can still remain large uncertainty in determining the accurate  
786 reconnection plane which can impact the reconnection rates, and therefore, the FTE growth rate  
787 provided in this study.

788  
789 It is concluded that the difference between the average FTE size observed at the subsolar  
790 magnetopause by MMS (*Akhavan-Tafti et al.*, 2018) and at high-latitude and flank regions by  
791 Cluster (e.g., *Wang et al.*, 2005; *Fermo et al.*, 2011) is most likely due to their orbits and different  
792 FTE sampling populations. As suggested by *Akhavan-Tafti et al.* (2018), FTEs grow while  
793 convecting away from the subsolar region where they are most likely formed. Therefore, MMS,  
794 due to its near-equatorial orbit, is expected to observe smaller-scale FTEs soon after formation,  
795 hence, smaller average FTE size compared to Cluster, due to its polar orbit. Further investigation  
796 of the Cluster magnetic field data is required to confirm this conclusion, since the study by *Wang*  
797 *et al.* (2005) did not account for small-scale FTEs (4s cadence magnetometer data).

798  
799 Characteristic scale lengths, including the ion inertial length, determine the micro-scale  
800 reconnection physics. However, simulating global simulation systems with a broad range of  
801 temporal and spatial dynamical scales remains quite challenging (e.g., *Tóth et al.*, 2017). The  
802 magnetosheath ion inertial length ( $d_i \sim 150$  km at the magnetopause under the stated upstream  
803 conditions) is not resolved in the Vlasiator's simulation grid (spatial grid resolution = 300 km)  
804 which may impact the micro-physics of reconnection, and therefore, the reconnection-driven  
805 dynamics and rates provided in this study. Nevertheless, Vlasiator is shown to capture  
806 reconnection ion kinetics, despite not resolving the relevant spatial scales. Future investigations  
807 shall revisit Vlasiator reconnection in simulations with improved spatial resolutions.

## 808 5. Conclusion

809 The hybrid-Vlasov Vlasiator simulations of multiple X-point reconnection at the subsolar region  
810 are compared with MMS observations of two neighboring X-lines within which at least five ion-  
811 scale FTEs are identified. The signatures of multiple X-line reconnection are found in both the  
812 Vlasiator simulations and the MMS observations. Non-isotropic ion distributions are observed in  
813 MMS observations in two possible reconnection inflow region encounters. These non-isotropic  
814 (crescent-shaped) ion distributions are in good agreement with the Vlasiator simulations,  
815 indicating that, despite not fully resolving the ion inertial length in the magnetosheath, the  
816 Vlasiator code captures key reconnection signatures.

817  
818 We further investigate the evolution of the Vlasiator's two-dimensional magnetic islands due to  
819 magnetic reconnection. Magnetic islands at the low-latitude magnetopause (polar angle,  $|\theta| < 30$   
820 degrees) are found to grow mainly due to continuous reconnection at adjacent X-points. It is also  
821 shown that magnetic islands further evolve due to coalescence, erosion, and division. The  
822 relationship between the normalized rate of reconnection at an adjacent X-point and the change in  
823 the islands' enclosed magnetic flux are determined.

824  
825 The average rate at which magnetic flux is added to the outer layers of magnetic islands due to  
826 continuous reconnection at adjacent X-points is determined. Based on our statistical analysis of  
827 magnetic islands in the Vlasiator code, magnetic islands grow at  $< +0.3 R_E^2/\text{min}$ . At this rate, a  
828 subsolar MMS-observed  $d_i$ -scale FTE is estimated to grow Earth-sized within  $\sim 10$  minutes while  
829 convecting away from the reconnection sites along the magnetopause. The estimated growth time  
830 is comparable to the average transport time for FTEs formed in the subsolar region to reach the  
831 high-latitude magnetopause and flanks. More importantly, the Vlasiator island statistics provide  
832 an equation for estimating the rate of FTE growth ( $\Delta A/\Delta t$ ) that is based on physical parameters  
833 that can be (directly or indirectly) measured by single or multi-spacecraft observations, including  
834 FTE size ( $A$ ), magnetic flux content ( $\psi$ ), and normalized reconnection rate ( $\mathcal{R}$ ). Vlasiator  
835 reconnection dynamics shall be revisited in future simulations with improved spatial resolutions.

836  
837 Finally, it is concluded that the discrepancy in the average FTE size at the magnetopause between  
838 the Cluster and MMS observations is most likely the result of their different orbits, wherein MMS  
839 mainly observes the newly-formed FTEs at the subsolar region near the magnetic equator while  
840 Cluster detects grown FTEs farther away from the subsolar region at higher-latitude magnetopause  
841 and flanks. Further investigation of the Cluster magnetic field measurements are required to  
842 confirm this conclusion.

843

844 **Acknowledgements**

845 The authors acknowledge the European Research Council for starting grant 200141-QuESpace,  
846 with which Vlasiator was developed, and Consolidator grant 682068-PRESTISSIMO awarded to  
847 further develop Vlasiator and use it for scientific investigations. The authors gratefully also  
848 acknowledge the Academy of Finland (grants 138599, 267144, and 309937) and the CSC-IT  
849 Center for Science Grand Challenge grant, and PRACE Tier-0 grant number 2014112573 with  
850 which the Vlasiator simulation run was carried out. Vlasiator  
851 (<http://www.physics.helsinki.fi/vlasiator/>) is distributed under the GPL-2 open source license  
852 (Palmroth et al., 2019). To learn more, see von Alfthan et al. (2020). Vlasiator uses a data structure  
853 developed in-house (Sandroos, 2019), which is compatible with the VisIt visualization software  
854 (*Childs*, 2012) using a plugin available at the VLSV repository. The Analysator software was used  
855 to produce the presented figures. The run described here takes several terabytes of disk space and  
856 is kept in storage maintained within the CSC IT Center for Science. Data presented in this paper  
857 can be accessed by following the data policy on the Vlasiator web site  
858 (<https://www.helsinki.fi/en/researchgroups/vlasiator/rules-of-the-road>). The authors would also  
859 like to thank the MMS team for providing high-quality data products and analysis tools. The data  
860 can be publicly accessed at the MMS Science Data Center website  
861 (<https://lasp.colorado.edu/mms/sdc/public/>). The work done at the University of Michigan was  
862 supported by NASA MMS contract NNG04EB99C at the Southwest Research Institute, NASA  
863 MMS GI grant 80NSSC18K1363, and NASA grant 80NSSC18K0999. The work done at École  
864 Polytechnique was supported by the DGA project, convention 2778/IMES.



865 **References**

- 866 Akhavan-Tafti, M., Slavin, J. A. A., Le, G., Eastwood, J. P. P., Strangeway, R. J., Russell, C. T.,  
867 ... Burch, J. L. (2018). MMS Examination of FTEs at the Earth's Subsolar Magnetopause.  
868 *Journal of Geophysical Research: Space Physics*. <https://doi.org/10.1002/2017JA024681>
- 869 Akhavan-Tafti, M., Slavin, J. A., Eastwood, J. P., Cassak, P. A., & Gershman, D. J. (2019).  
870 MMS Multi-Point Analysis of FTE Evolution: Physical Characteristics and Dynamics.  
871 *Journal of Geophysical Research: Space Physics*. <https://doi.org/10.1029/2018JA026311>
- 872 Akhavan-Tafti, M., Slavin, J. A., Sun, W. J., Le, G., & Gershman, D. J. (2019). MMS  
873 Observations of Plasma Heating Associated with FTE Growth. *Geophysical Research*  
874 *Letters*, *46*.
- 875 von Alfthan, S., Pokhotelov, D., Kempf, Y., Hoilijoki, S., Honkonen, I., Sandroos, A., &  
876 Palmroth, M. (2014). Vlasiator: First global hybrid-Vlasov simulations of Earth's foreshock  
877 and magnetosheath. *Journal of Atmospheric and Solar-Terrestrial Physics*, *120*, 24–35.
- 878 von Alfthan, S., Pfau-Kempf, Y., Sandroos, A., Ganse, U., Hannuksela, O. A., Honkonen, I., ...  
879 Pokhotelov, D. (2020). fmihpc/vlasiator: Vlasiator. *Zenodo*.  
880 <https://doi.org/10.5281/zenodo.3640593>
- 881 Aunai, N., Hesse, M., & Kuznetsova, M. (2013). Electron nongyrotropy in the context of  
882 collisionless magnetic reconnection. *Physics of Plasmas*, *20*(9), 92903.
- 883 Bessho, N., Chen, L.-J., & Hesse, M. (2016). Electron distribution functions in the diffusion  
884 region of asymmetric magnetic reconnection. *Geophysical Research Letters*, *43*(5), 1828–  
885 1836.
- 886 Burch, J. L., & Phan, T. D. (2016). Magnetic reconnection at the dayside magnetopause:  
887 Advances with MMS. *Geophysical Research Letters*.  
888 <https://doi.org/10.1002/2016GL069787>
- 889 Burch, J L, Moore, T. E., Torbert, R. B., & Giles, B. L. (2016). Magnetospheric multiscale  
890 overview and science objectives. *Space Science Reviews*, *199*(1–4), 5–21.
- 891 Burch, J L, Torbert, R. B., Phan, T. D., Chen, L., Moore, T. E., Ergun, R. E., ... Goodrich, K. A.  
892 (2016). Electron-scale measurements of magnetic reconnection in space, *2939*(May).
- 893 Burch, James L., Torbert, R. B., Phan, T. D., Chen, L.-J., Moore, T. E., Ergun, R. E., ... Others.  
894 (2016). Electron-scale measurements of magnetic reconnection in space. *Science*,  
895 *352*(6290), aaf2939.
- 896 Cassak, P. A., & Shay, M. A. (2007). Scaling of asymmetric magnetic reconnection: General  
897 theory and collisional simulations. *Physics of Plasmas*, *14*(10), 102114.
- 898 Cassak, P. A., Liu, Y.-H., & Shay, M. A. (2017). A review of the 0.1 reconnection rate problem.  
899 *Journal of Plasma Physics*, *83*(5).
- 900 Che, H., Schiff, C., Le, G., Dorelli, J. C., Giles, B. L., & Moore, T. E. (2018). Quantifying the  
901 effect of non-Larmor motion of electrons on the pressure tensor. *Physics of Plasmas*, *25*(3),  
902 32101.
- 903 Chen, L.-J., Hesse, M., Wang, S., Gershman, D., Ergun, R. E., Burch, J., ... others. (2017).  
904 Electron diffusion region during magnetopause reconnection with an intermediate guide  
905 field: Magnetospheric multiscale observations. *Journal of Geophysical Research: Space*  
906 *Physics*, *122*(5), 5235–5246.
- 907 Chen, Y., Tóth, G., Cassak, P., Jia, X., Gombosi, T. I., Slavin, J. A., ... Henderson, M. G.  
908 (2017). Global Three-Dimensional Simulation of Earth's Dayside Reconnection Using a  
909 Two-Way Coupled Magnetohydrodynamics With Embedded Particle-in-Cell Model: Initial  
910 Results. *Journal of Geophysical Research: Space Physics*, *122*(10), 10,318-10,335.

911 <https://doi.org/10.1002/2017JA024186>  
912 Childs, H., Brugger, E., Whitlock, B., Meredith, J., Ahern, S., Pugmire, D., Biagas, K., Miller,  
913 M., Harrison, C., Weber, G. H., Krishnan, H., Fogal, T., Sanderson, A., Garth, C., Bethel, E.  
914 W., Camp, D., Rübél, O., Favre, M. J., & Durant Navr'atil, P. (2012). VisIt: An end-user  
915 tool for visualizing and analyzing very large data, High performance visualization-enabling  
916 extreme-scale scientific insight (pp. 357–372). Boca Raton, Florida: Chapman & Hall /  
917 CRC.  
918 Cowley, S. W. H. (1995). Theoretical perspectives of the magnetopause: A tutorial review.  
919 *Physics of the Magnetopause*, 90, 29–43.  
920 Daldorff, L. K. S., Tóth, G., Gombosi, T. I., Lapenta, G., Amaya, J., Markidis, S., & Brackbill, J.  
921 U. (2014). Two-way coupling of a global Hall magnetohydrodynamics model with a local  
922 implicit particle-in-cell model. *Journal of Computational Physics*, 268, 236–254.  
923 Daughton, W., Roytershteyn, V., Albright, B. J., Karimabadi, H., Yin, L., & Bowers, K. J.  
924 (2009). Transition from collisional to kinetic regimes in large-scale reconnection layers.  
925 *Physical Review Letters*, 103(6), 065004. <https://doi.org/10.1103/PhysRevLett.103.065004>  
926 Daughton, W., Roytershteyn, V., Karimabadi, H., Yin, L., Albright, B. J., Bergen, B., & Bowers,  
927 K. J. (2011). Role of electron physics in the development of turbulent magnetic  
928 reconnection in collisionless plasmas. *Nature Physics*, 7(7), 539–542.  
929 <https://doi.org/10.1038/nphys1965>  
930 Dorelli, J. C., & Bhattacharjee, A. (2009). On the generation and topology of flux transfer  
931 events. *Journal of Geophysical Research: Space Physics*, 114(6), 1–21.  
932 <https://doi.org/10.1029/2008JA013410>  
933 Eastwood, J. P., Phan, T. D., Fear, R. C., Sibeck, D. G., Angelopoulos, V., Ieroset, M., ... Shay,  
934 M. A. (2012). Survival of flux transfer event (FTE) flux ropes far along the tail  
935 magnetopause. *Journal of Geophysical Research: Space Physics*, 117(8), 1–9.  
936 <https://doi.org/10.1029/2012JA017722>  
937 Eastwood, J. P., Phan, T. D., Cassak, P. A., Gershman, D. J., Haggerty, C., Malakit, K., ...  
938 Wang, S. (2016). Ion-scale secondary flux-ropes generated by magnetopause reconnection  
939 as resolved by MMS. *Geophysical Research Letters*, 43(10), 1–9.  
940 <https://doi.org/10.1002/2016GL068747>  
941 Egedal, J., Le, A., Pritchett, P. L., & Daughton, W. (2011). Electron dynamics in two-  
942 dimensional asymmetric anti-parallel reconnection. *Physics of Plasmas*, 18(10), 102901.  
943 Ergun, R. E., Tucker, S., Westfall, J., Goodrich, K. A., Malaspina, D. M., Summers, D., ...  
944 Cully, C. M. (2016). The axial double probe and fields signal processing for the MMS  
945 mission. *Space Science Reviews*, 199(1–4), 167–188. [https://doi.org/10.1007/s11214-014-](https://doi.org/10.1007/s11214-014-0115-x)  
946 [0115-x](https://doi.org/10.1007/s11214-014-0115-x)  
947 Fear, R. C., Milan, S. E., Fazakerley, A. N., Lucek, E. A., Cowley, S. W. H., & Dandouras, I.  
948 (2008). The azimuthal extent of three flux transfer events. *Annales Geophysicae*, 26(8),  
949 2353–2369. <https://doi.org/10.5194/angeo-26-2353-2008>  
950 Fermo, R. ~L. L., Drake, J. ~F. F., & Swisdak, M. (2010). A statistical model of magnetic  
951 islands in a current layer. *Physics of Plasmas*, 17(1), 10702.  
952 <https://doi.org/10.1063/1.3286437>  
953 Fermo, R. L., Drake, J. F., Swisdak, M., & Hwang, K. J. (2011). Comparison of a statistical  
954 model for magnetic islands in large current layers with Hall MHD simulations and Cluster  
955 FTE observations. *Journal of Geophysical Research: Space Physics*, 116(A9), n/a-n/a.  
956 <https://doi.org/10.1029/2010ja016271>

- 957 Fuselier, S. A., Petrinec, S. M., Trattner, K. J., Broll, J. M., Burch, J. L., Giles, B. L., ... others.  
958 (2018). Observational Evidence of Large-Scale Multiple Reconnection at the Earth's  
959 Dayside Magnetopause. *Journal of Geophysical Research: Space Physics*, 123(10), 8407–  
960 8421.
- 961 Fuselier, S. A., Trattner, K. J., Petrinec, S. M., Owen, C. J., & Rème, H. (2005). Computing the  
962 reconnection rate at the Earth's magnetopause using two spacecraft observations. *Journal of*  
963 *Geophysical Research: Space Physics*, 110(A6).
- 964 Gary, S. P., Fuselier, S. A., & Anderson, B. J. (1993). Ion Anisotropy Instabilities in the  
965 Magnetosheath. *JOURNAL OF GEOPHYSICAL RESEARCH*, 98(1), 1481–1488.  
966 <https://doi.org/10.1029/92JA01844>
- 967 Genestreti, K. J., Nakamura, T. K. M., Nakamura, R., Denton, R. E., Torbert, R. B., Burch, J. L.,  
968 ... others. (2018). How Accurately Can We Measure the Reconnection Rate EM for the  
969 MMS Diffusion Region Event of 11 July 2017? *Journal of Geophysical Research: Space*  
970 *Physics*, 123(11), 9130–9149.
- 971 Grandin, M., Battarbee, M., Osmane, A., Ganse, U., Pfau-Kempf, Y., Turc, L., ... Palmroth, M.  
972 (2019). Hybrid-Vlasov modelling of nightside auroral proton precipitation during southward  
973 interplanetary magnetic field conditions. In *Annales Geophysicae* (Vol. 37, pp. 791–806).
- 974 Harvey, C. C. (1998). Spatial Gradients and the Volumetric Tensor. Retrieved from  
975 <http://www.issibern.ch/forads/sr-001-12.pdf>
- 976 Hasegawa, H., Wang, J., Dunlop, M. W., Pu, Z. Y., Zhang, Q.-H. Q.-H. H., Lavraud, B., ...  
977 Bogdanova, Y. V. (2010). Evidence for a flux transfer event generated by multiple X-line  
978 reconnection at the magnetopause. *Geophysical Research Letters*, 37(16), 1–6.  
979 <https://doi.org/10.1029/2010GL044219>
- 980 Hasegawa, Hiroshi, Kitamura, N., Saito, Y., Nagai, T., Shinohara, I., Yokota, S., ... others.  
981 (2016). Decay of mesoscale flux transfer events during quasi-continuous spatially extended  
982 reconnection at the magnetopause. *Geophysical Research Letters*, 43(10), 4755–4762.  
983 <https://doi.org/10.1002/2016GL069225>
- 984 Hesse, M., Aunai, N., Sibeck, D., & Birn, J. (2014). On the electron diffusion region in planar,  
985 asymmetric, systems. *Geophysical Research Letters*, 41(24), 8673–8680.  
986 <https://doi.org/10.1002/2014GL061586>
- 987 Hoilijoki, S., Ganse, U., Sibeck, D. G., Cassak, P. A., Turc, L., Battarbee, M., ... others. (2019).  
988 Properties of magnetic reconnection and FTEs on the dayside magnetopause with and  
989 without positive IMF B component during southward IMF. *Journal of Geophysical*  
990 *Research: Space Physics*.
- 991 Hoilijoki, Sanni, Ganse, U., Pfau-Kempf, Y., Cassak, P. A., Walsh, B. M., Hietala, H., ...  
992 Palmroth, M. (2017). Reconnection rates and X line motion at the magnetopause: Global  
993 2D-3V hybrid-Vlasov simulation results. *Journal of Geophysical Research: Space Physics*,  
994 122(3), 2877–2888.
- 995 Hwang, K.-J., Sibeck, D. G., Burch, J. L., Choi, E., Fear, R. C., Lavraud, B., ... others. (2018).  
996 Small-scale flux transfer events formed in the reconnection exhaust region between two X-  
997 lines. *Journal of Geophysical Research: Space Physics*.
- 998 Hwang, K. J., Sibeck, D. G., Burch, J. L., Choi, E., Fear, R. C., Lavraud, B., ... Strangeway, R.  
999 J. (2018). Small-Scale Flux Transfer Events Formed in the Reconnection Exhaust Region  
1000 Between Two X Lines. *Journal of Geophysical Research: Space Physics*, 123(10), 8473–  
1001 8488. <https://doi.org/10.1029/2018JA025611>
- 1002 Imber, S. M., Slavin, J. A., Boardsen, S. A., Anderson, B. J., Korth, H., McNutt, R. L., &

1003 Solomon, S. C. (2014). MESSENGER observations of large dayside flux transfer events:  
1004 Do they drive Mercury's substorm cycle? *Journal of Geophysical Research: Space*  
1005 *Physics*, 119(7), 5613–5623. <https://doi.org/10.1002/2014JA019884>  
1006 Jarvinen, R., Vainio, R., Palmroth, M., Juusola, L., Hoilijoki, S., Pfau-Kempf, Y., ... von  
1007 Alfthan, S. (2018). Ion Acceleration by Flux Transfer Events in the Terrestrial  
1008 Magnetosheath. *Geophysical Research Letters*, 45(4), 1723–1731.  
1009 Jasinski, J. M., Slavin, J. A., Arridge, C. S., Poh, G., Jia, X., Sergis, N., ... Waite, J. H. (2016).  
1010 Flux transfer event observation at Saturn's dayside magnetopause by the Cassini spacecraft.  
1011 *Geophysical Research Letters*, 43(13), 6713–6723.  
1012 Juusola, L., Pfau-Kempf, Y., Ganse, U., Battarbee, M., Brito, T., Grandin, M., ... others. (2018).  
1013 A possible source mechanism for magnetotail current sheet flapping. In *Annales*  
1014 *Geophysicae*.  
1015 Juusola, L., Hoilijoki, S., Pfau-Kempf, Y., Ganse, U., Järvinen, R., Battarbee, M., ... others.  
1016 (2018). Fast plasma sheet flows and X line motion in the Earth's magnetotail. In *Annales*  
1017 *Geophysicae*.  
1018 Lapenta, G., Berchem, J., Zhou, M., Walker, R. J., El-Alaoui, M., Goldstein, M. L., ... Burch, J.  
1019 L. (2017). On the origin of the crescent-shaped distributions observed by MMS at the  
1020 magnetopause. *Journal of Geophysical Research: Space Physics*, 122(2), 2024–2039.  
1021 <https://doi.org/10.1002/2016JA023290>  
1022 Lee, L. C., & Fu, Z. F. (1985). A theory of magnetic flux transfer at the Earth's magnetopause.  
1023 *Geophysical Research Letters*, 12(2), 105–108. <https://doi.org/10.1029/GL012i002p00105>  
1024 Lindqvist, P.-A. P.-A., Olsson, G., Torbert, R. B., King, B., Granoff, M., Rau, D., ... others.  
1025 (2016). The spin-plane double probe electric field instrument for MMS. *Space Science*  
1026 *Reviews*, 199(1–4), 137–165. <https://doi.org/10.1007/s11214-014-0116-9>  
1027 Liu, Y.-H., Hesse, M., Guo, F., Daughton, W., Li, H., Cassak, P. A., & Shay, M. A. (2017). Why  
1028 does steady-state magnetic reconnection have a maximum local rate of order 0.1? *Physical*  
1029 *Review Letters*, 118(8), 85101.  
1030 Lu, S., Lu, Q., Lin, Y., Wang, X., Ge, Y., Wang, R., ... others. (2015). Dipolarization fronts as  
1031 earthward propagating flux ropes: A three-dimensional global hybrid simulation. *Journal of*  
1032 *Geophysical Research: Space Physics*, 120(8), 6286–6300.  
1033 Ma, Z. W. T., Otto, A., & Lee, L. C. (1994). Core magnetic field enhancement in single X line,  
1034 multiple X line and patchy reconnection. *Journal of Geophysical Research: Space Physics*,  
1035 99(A4), 6125–6136.  
1036 Malakit, K., Shay, M. A., Cassak, P. A., & Ruffolo, D. (2013). New electric field in asymmetric  
1037 magnetic reconnection. *Physical Review Letters*, 111(13), 135001.  
1038 Man, H. Y., Zhou, M., Deng, X. H., Fu, H. S., Zhong, Z. H., Chen, Z. Z., ... others. (2018). In  
1039 situ observation of magnetic reconnection between an earthward propagating flux rope and  
1040 the geomagnetic field. *Geophysical Research Letters*, 45(17), 8729–8737.  
1041 Markidis, S., Henri, P., Lapenta, G., Divin, A., Goldman, M., Newman, D., & Laure, E. (2013).  
1042 Kinetic simulations of plasmoid chain dynamics. *Physics of Plasmas*, 20(8), 82105.  
1043 MMS Examination of FTEs at the Earth's Subsolar Magnetopause. (n.d.).  
1044 Motschmann, U., Glassmeier, K. H., & Brinca, A. L. (1999). Nongyrotropic particle distributions  
1045 in space plasmas. In *Annales Geophysicae* (Vol. 17, pp. 613–622).  
1046 Mozer, F. S., Bale, S. D., & Phan, T. D. (2002). Evidence of diffusion regions at a subsolar  
1047 magnetopause crossing. *Physical Review Letters*, 89(1), 15002.  
1048 Nagai, T., Shinohara, I., & Zenitani, S. (2015). Ion acceleration processes in magnetic

1049 reconnection: Geotail observations in the magnetotail. *Journal of Geophysical Research: Space Physics*, 120(3), 1766–1783. <https://doi.org/10.1002/2014JA020737>

1050

1051 Øieroset, M., Phan, T. D., Eastwood, J. P., Fujimoto, M., Daughton, W., Shay, M. A., ...

1052 Glassmeier, K.-H. H. (2011). Direct evidence for a three-dimensional magnetic flux rope

1053 flanked by two active magnetic reconnection X lines at earth's magnetopause. *Physical*

1054 *Review Letters*, 107(16), 165007. <https://doi.org/10.1103/PhysRevLett.107.165007>

1055 Øieroset, M., Phan, T. D., Drake, J. F., Eastwood, J. P., Fuselier, S. A., Strangeway, R. J., ...

1056 others. (2019). Reconnection With Magnetic Flux Pileup at the Interface of Converging Jets

1057 at the Magnetopause. *Geophysical Research Letters*, 46(4), 1937–1946.

1058 Owen, C. J., Fazakerley, A. N., Carter, P. J., Coates, A. J., Krauklis, I. C., Szita, S., ... Dunlop,

1059 M. W. (2001). Cluster PEACE observations of electrons during magnetospheric flux

1060 transfer events. *Annales Geophysicae*, 19(10/12), 1509–1522. Retrieved from

1061 <https://hal.archives-ouvertes.fr/hal-00316948/#.VdJIssFtcS8.mendeley>

1062 Palmroth, M., Praks, J., Vainio, R., Janhunen, P., Kilpua, E. K. J., Afanasiev, A., ... Westerlund,

1063 T. (2019). FORESAIL-1 CubeSat Mission to Measure Radiation Belt Losses and

1064 Demonstrate Deorbiting. *Journal of Geophysical Research: Space Physics*, 1–17.

1065 <https://doi.org/10.1029/2018ja026354>

1066 Palmroth, M., Honkonen, I., Sandroos, A., Kempf, Y., von Alfthan, S., & Pokhotelov, D. (2013).

1067 Preliminary testing of global hybrid-Vlasov simulation: Magnetosheath and cusps under

1068 northward interplanetary magnetic field. *Journal of Atmospheric and Solar-Terrestrial*

1069 *Physics*, 99, 41–46.

1070 Palmroth, Minna, Ganse, U., Pfau-Kempf, Y., Battarbee, M., Turc, L., Brito, T., ... von Alfthan,

1071 S. (2018). Vlasov methods in space physics and astrophysics. *Living Reviews in*

1072 *Computational Astrophysics*, 4(1), 1.

1073 Palmroth, Minna, Hoilijoki, S., Juusola, L., Pulkkinen, T. I., Hietala, H., Pfau-Kempf, Y., ...

1074 others. (2017). Tail reconnection in the global magnetospheric context. In *Annales*

1075 *Geophysicae*.

1076 Paschmann, G., Haerendel, G., Papamastorakis, I., Sckopke, N., Bame, S. J., Gosling, J. T., &

1077 Russell, C. T. (1982). Plasma and magnetic field characteristics of magnetic flux transfer

1078 events. *Journal of Geophysical Research*, 87(A4), 2159.

1079 <https://doi.org/10.1029/JA087iA04p02159>

1080 Pfau-Kempf, Y., Battarbee, M., Ganse, U., Hoilijoki, S., Turc, L., von Alfthan, S., ... Palmroth,

1081 M. (2018). On the importance of spatial and velocity resolution in the hybrid-Vlasov

1082 modeling of collisionless shocks. *Frontiers in Physics*, 6, 44.

1083 Phan, T. D., Dunlop, M. W., Paschmann, G., Klecker, B., Bosqued, J. M., Reme, H., ... Kistler,

1084 L. M. (2004). Cluster observations of continuous reconnection at the magnetopause under

1085 steady interplanetary magnetic field conditions. In *Annales Geophysicae* (Vol. 22, pp.

1086 2355–2367). Copernicus GmbH. <https://doi.org/10.5194/angeo-22-2355-2004>

1087 Phan, T. D., Paschmann, G., Twitty, C., Mozer, F. S., Gosling, J. T., Eastwood, J. P., ... Lucek,

1088 E. A. (2007). Evidence for magnetic reconnection initiated in the magnetosheath.

1089 *Geophysical Research Letters*, 34(14).

1090 Poh, G., Slavin, J. A., Lu, S., Le, G., Ozturk, D. S., Sun, W.-J., ... Burch, J. L. (2019).

1091 Dissipation of Earthward Propagating Flux Rope Through Re-reconnection with

1092 Geomagnetic Field: An MMS Case Study. *Journal of Geophysical Research: Space*

1093 *Physics*. <https://doi.org/10.1029/2018JA026451>

1094 Pollock, C., Moore, T., Jacques, A., Burch, J., Gliese, U., Saito, Y., ... Zeuch, M. (2016). Fast

1095 Plasma Investigation for Magnetospheric Multiscale. *Space Science Reviews*, 199(1–4),  
1096 331–406. <https://doi.org/10.1007/s11214-016-0245-4>

1097 Pritchett, P. L., & Mozer, F. S. (2009). The magnetic field reconnection site and dissipation  
1098 region. *Physics of Plasmas*, 16(8), 80702.

1099 Pritchett, P. L., & Wu, C. C. (1979). Coalescence of magnetic islands. *The Physics of Fluids*,  
1100 22(11), 2140–2146.

1101 Raeder, J. (2006). Flux transfer events: 1. Generation mechanism for strong southward IMF. In  
1102 *Annales Geophysicae* (Vol. 24, pp. 381–392).

1103 Russell, C. T., Anderson, B. J., Baumjohann, W., Bromund, K. R., Dearborn, D., Fischer, D., ...  
1104 Richter, I. (2016). The Magnetospheric Multiscale Magnetometers. *Space Science Reviews*,  
1105 199(1–4), 189–256. <https://doi.org/10.1007/s11214-014-0057-3>

1106 Sandroos, A. (2019). Vlsv: File format and tools. Github repository. Retrieved  
1107 from <https://github.com/fmihpc/vlsv/> (last access: 09.05.2019).

1108 Slavin, J. A., Lepping, R. P., Gjerloev, J., Fairfield, D. H., Hesse, M., Owen, C. J., ... Mukai, T.  
1109 (2003). Geotail observations of magnetic flux ropes in the plasma sheet. *Journal of*  
1110 *Geophysical Research*, 108(A1), 1015. <https://doi.org/10.1029/2002JA009557>

1111 Slavin, J A, Owen, C. J., Kuznetsova, M. M., & Hesse, M. (1995). ISEE 3 observations of  
1112 plasmoids with flux rope magnetic topologies. *Geophysical Research Letters*, 22(15),  
1113 2061–2064.

1114 Slavin, James A, Acuña, M. H., Anderson, B. J., Baker, D. N., Benna, M., Boardsen, S. A., ...  
1115 others. (2009). MESSENGER observations of magnetic reconnection in Mercury's  
1116 magnetosphere. *Science*, 324(5927), 606–610.

1117 Sonnerup, B. U. Ö., Paschmann, G., Papamastorakis, I., Sckopke, N., Haerendel, G., Bame, S. J.,  
1118 ... Russell, C. T. (1981). Evidence for magnetic field reconnection at the Earth's  
1119 magnetopause. *Journal of Geophysical Research: Space Physics*, 86(A12), 10049–10067.

1120 Sun, W. J., Slavin, J. A., Tian, A. M., Bai, S. C., Poh, G. K., Akhavan-Tafti, M., ... others.  
1121 (2019). MMS study of the structure of ion-scale flux ropes in the Earth's cross-tail current  
1122 sheet. *Geophysical Research Letters*.

1123 Swisdak, M. (2016). Quantifying gyrotropy in magnetic reconnection. *Geophysical Research*  
1124 *Letters*, 43(1), 43–49.

1125 Torbert, R. B., Russell, C. T., Magnes, W., Ergun, R. E., Lindqvist, P.-A., LeContel, O., ...  
1126 Lappalainen, K. (2016). The FIELDS Instrument Suite on MMS: Scientific Objectives,  
1127 Measurements, and Data Products. *Space Science Reviews*, 199(1–4), 105–135.  
1128 <https://doi.org/10.1007/s11214-014-0109-8>

1129 Tóth, G., Chen, Y., Gombosi, T. I., Cassak, P., Markidis, S., & Peng, I. B. (2017). Scaling the  
1130 ion inertial length and its implications for modeling reconnection in global simulations.  
1131 *Journal of Geophysical Research: Space Physics*, 122(10).

1132 Trattner, K. J., Petrinec, S. M., Fuselier, S. A., Omidi, N., & Sibeck, D. G. (2012). Evidence of  
1133 multiple reconnection lines at the magnetopause from cusp observations. *Journal of*  
1134 *Geophysical Research: Space Physics*, 117(A1).

1135 Uzdensky, D. A., Loureiro, N. F., & Schekochihin, A. A. (2010). Fast Magnetic Reconnection in  
1136 the Plasmoid-Dominated Regime. *Physical Review Letters*, 105(23), 235002.  
1137 <https://doi.org/10.1103/PhysRevLett.105.235002>

1138 Walker, R. J., & Russell, C. T. (1985). Flux transfer events at the Jovian magnetopause. *Journal*  
1139 *of Geophysical Research: Space Physics*, 90(A8), 7397–7404.

1140 Wang, R., Lu, Q., Nakamura, R., Huang, C., Du, A., Guo, F., ... Wang, S. (2016). Coalescence

1141 of magnetic flux ropes in the ion diffusion region of magnetic reconnection. *Nature Physics*,  
1142 12(3), 263–267. <https://doi.org/10.1038/nphys3578>  
1143 Wang, S., Chen, L.-J., Hesse, M., Bessho, N., Gershman, D. J., Dorelli, J., ... others. (2016).  
1144 Two-scale ion meandering caused by the polarization electric field during asymmetric  
1145 reconnection. *Geophysical Research Letters*, 43(15), 7831–7839.  
1146 Wang, Y. L., Elphic, R. C., Lavraud, B., Taylor, M. G. G. T., Birn, J., Raeder, J., ... Friedel, R.  
1147 H. (2005). Initial results of high-latitude magnetopause and low-latitude flank flux transfer  
1148 events from 3 years of Cluster observations. *Journal of Geophysical Research: Space*  
1149 *Physics*, 110(A11), 1–10. <https://doi.org/10.1029/2005JA011150>  
1150 Wang, Y. L., Elphic, R. C., Lavraud, B., Taylor, M., Birn, J., Russell, C. T., ... Zhang, X. X.  
1151 (2006). Dependence of flux transfer events on solar wind conditions from 3 years of Cluster  
1152 observations. *Journal of Geophysical Research: Space Physics*, 111(A4).  
1153 Yamada, M., Ono, Y., Hayakawa, A., Katsurai, M., & Perkins, F. W. (1990). Magnetic  
1154 reconnection of plasma toroids with cohelicity and counterhelicity. *Physical Review Letters*,  
1155 65(6), 721.  
1156 Yeates, A. R., & Hornig, G. (2011). Dynamical constraints from field line topology in magnetic  
1157 flux tubes. *Journal of Physics A: Mathematical and Theoretical*, 44(26), 265501.  
1158 Zhang, H., Kivelson, M. G., Khurana, K. K., McFadden, J., Walker, R. J., Angelopoulos, V., ...  
1159 others. (2010). Evidence that crater flux transfer events are initial stages of typical flux  
1160 transfer events. *Journal of Geophysical Research: Space Physics*, 115(A8).  
1161 <https://doi.org/10.1029/2009JA015013>  
1162 Zhao, Y., Wang, R., Lu, Q., Du, A., Yao, Z., & Wu, M. (2016). Coalescence of magnetic flux  
1163 ropes observed in the tailward high-speed flows. *Journal of Geophysical Research: Space*  
1164 *Physics*, 121(11), 10,898–10,909. <https://doi.org/10.1002/2016JA023526>  
1165 Zhou, M., Berchem, J., Walker, R. J. J., El-Alaoui, M., Deng, X., Cazzola, E., ... Burch, J. L.  
1166 (2017). Coalescence of Macroscopic Flux Ropes at the Subsolar Magnetopause:  
1167 Magnetospheric Multiscale Observations. *Physical Review Letters*, 119(5), 055101.  
1168 <https://doi.org/10.1103/PhysRevLett.119.055101>  
1169

1170 **Figures**

1171

1172 **Figure 1:** Two dimensional schematics of ion flows in a typical FTE forming due to multiple X-  
1173 line reconnection. Field-aligned currents (FACs; white-red arrows) are generated due to  
1174 reconnection. Inflowing ions ( $V_{in}$ ; green arrow) are also accelerated inside the ion diffusion region  
1175 (IDR) perpendicular to the magnetic field ( $V_{out}$ ; red arrow) downstream of an X-line. The  
1176 reconnecting field lines, i.e., separatrices, are shown as dashed lines.

1177 **Figure 2:** Schematic of magnetic island dynamics driven by magnetic reconnection. The enclosed  
1178 area,  $A$ , inside magnetic islands increases due to coalescence and continuous reconnection at  
1179 adjacent X-lines. The island's magnetic flux content,  $\psi$ , changes due to magnetic reconnection.  
1180 The arrows indicate island convection flows, wherein the inflow is shown in black solid arrows  
1181 and the outflows are presented as white arrows. Last reconnected field lines are indicated as bold  
1182 solid lines. The dashed lines represent magnetic separatrices which embody reconnecting field  
1183 lines.

1184 **Figure 3:** Three simulation timeframes (simulation box:  $6 < X \text{ [RE]} < 11$  and  $-1 < Z \text{ [RE]} < 4$  at  $t$   
1185 = 2106.0, 2119.0, and 2131.0 seconds since the simulation initialization) to illustrate the temporal  
1186 evolution of a magnetic island in the northern hemisphere magnetosheath. The color bar indicates  
1187  $E_x$ . The magenta 'X' markers indicate the X-points, i.e., saddle points in the magnetic flux  
1188 function. The reconnecting field lines are shown in green. The newly formed magnetic island  
1189 located between X1 and X2 is shown in cyan. The dashed lines in panel b provide two virtual  
1190 spacecraft trajectories, T1 and T2.

1191 **Figure 4:** Vlasiator electric field profiles and ion velocity distribution functions across X1 and X2  
1192 along two virtual spacecraft trajectories, T1 and T2. The panels include: a&b)  $E_x$  profile (black  
1193 solid curve) along virtual spacecraft T1, including the Ohm's law components, in particular, the  
1194 convection term ( $-V \times B$ ; red solid curve) and the Hall term ( $J \times B / ne$ ; blue solid curve), and 1-3) ion  
1195 VDFs sliced in the  $V_B - V_{B \times V}$  and 4-6)  $V_{B \times V} - V_{B \times (B \times V)}$  planes, where  $V_B$  represents the velocity  
1196 along the magnetic field orientation,  $V_{B \times V}$  and  $V_{B \times (B \times V)}$ , respectively, along  $(B \times V)$  and  
1197  $B \times (B \times V)$  directions, where  $V$  is the ion bulk velocity. The ion VDFs are generated at different  
1198  $E_x$  extrema and marked with vertical green solid lines. The X-point crossing is marked with a  
1199 vertical magenta dashed line. Two videos illustrating the temporal evolutions of ion VDFs as a  
1200 function of  $E_x$  and position with respect to X1 and X2 are included in supplementary **Video S1** and  
1201 **Video S2**, respectively.

1202  
1203 **Figure 5:** Temporal profile of the normalized reconnection rate,  
1204  $\mathcal{R} = E_y^{x\text{-point}} v_{Ai}^{-1} B^{-1}$ , at the X1 and X2, in the reference frame of the X-points. The vertical grey  
1205 line indicates the simulation timeframe  $t = 2119.0$  s.

1206  
1207 **Figure 6:** a) Example snapshot (simulation timeframe:  $t = 2119.0$  s) of the Vlasiator  
1208 magnetopause. The 'X'-points and 'O'-points are automatically identified by the algorithm. The  
1209 color bar indicates the electric field along the  $X_{GSM}$  axis,  $E_x$  [mV/m]. b) Magnetic islands  
1210 categorized into four quadrants, Q1-4, based on their temporal change in enclosed magnetic flux,  
1211  $\Delta\psi$ , and cross-sectional area,  $\Delta A$ . The linear fit from the orthogonal distance regression, shown as  
1212 dashed black line, is  $y = 2.16x - 0.03$ . The color bars indicate the count of events per bin. c) The  
1213 change in the enclosed magnetic flux as a function of normalized reconnection rate,



1214  $\mathcal{R} = E_y^{x-point} v_{Ai}^{-1} B^{-1}$ . The linear fit from the orthogonal distance regression, shown as dashed black  
1215 line, is  $y = 8.6x - 0.5$ . The red circles denote coalescing magnetic islands wherein two neighboring  
1216 magnetic islands merge and create one larger island.

1217  
1218 **Figure 7:** Magnetic field and plasma moments as observed at the barycenter of the four MMS  
1219 spacecraft for a magnetopause crossing of December 14, 2015 — 00:57:40 - 01:00:10 UT. The  
1220 panels include: a) total magnetic field, b) magnetic field components in the Geocentric Solar  
1221 Ecliptic (GSE) coordinates, c) ion plasma density, d) ion velocity components, e) electron velocity  
1222 components, f) parallel (red solid line) and perpendicular (black solid line) current density  
1223 components, g) parallel (red solid line) and perpendicular (black solid line) ion temperature  
1224 components, h) plasma beta  $\beta$ , defined as the ratio of plasma thermal pressure to magnetic pressure.  
1225 The magenta-shaded bars indicate the locations of FTEs. The cyan bar indicates the location of a  
1226 possible reconnection inflow crossing.





1227 **Figure 8:** Schematic of the approximate locations and orientations of the observed ion-scale FTEs,  
1228 shown as out-of-plane cylinders wherein the magnetic field intensity enhances (darker shade) near  
1229 the FTE core regions, and the adjacent reconnection X-lines, in the FTE's frame of reference and  
1230 in the LMN coordinates. The X-lines are marked by dashed lines. The magnetosheath and  
1231 magnetospheric magnetic flux are distinguished and shown as red and blue-shaded surfaces,  
1232 respectively. The MMS spacecraft trajectory, shown as a black arrow traversing across the  
1233 structures is estimated based on the MMS observations. The blue (B) and red (A) arrows/panels  
1234 represent ion velocity distribution slices in the vicinity of the two observed X-lines at 00:58:26  
1235 and 00:59:15 UT, respectively. The energy bins are divided into four energy bins organized in two  
1236 rows: *panels 1-4*) the  $\mathbf{V}_B - \mathbf{V}_{B \times V}$  slice, and *panels 5-8*) the  $\mathbf{V}_{B \times V} - \mathbf{V}_{B \times (B \times V)}$  slice, where  $\mathbf{V}_B$   
1237 represents the velocity along the magnetic field orientation.  $\mathbf{V}_{B \times V}$  and  $\mathbf{V}_{B \times (B \times V)}$  are along  $(\mathbf{B} \times \mathbf{V})$   
1238 and  $\mathbf{B} \times (\mathbf{B} \times \mathbf{V})$  directions, where  $\mathbf{V}$  is the ion bulk velocity. The energy bins include: *panels 1&5*)  
1239 1 eV-30 keV, *panels 2&6*) 1 eV – 3 keV, *panels 3&7*) 3-6 keV, and *panels 4&8*) 6-30 keV. The  
1240 ion bulk velocity is subtracted from the velocity distribution functions.

1241 **Figure 9:** Fields and plasma moments in the vicinity of a possible reconnection inflow crossing in  
1242 LMN coordinates as observed by MMS 1: a) magnetic field magnitude,  $|\mathbf{B}|$ , b) magnetic field  
1243 components, c) ion velocity components, d) electron velocity components, e) electric field  
1244 components in the spacecraft's frame of reference, f) corrected electric field components in the  
1245 current sheet's frame of reference, and g) Alfvén velocity. The normalized reconnection rate is  
1246 estimated from the fields and plasma signatures in the purple-shaded region.

1247  
1248 **Table I:** The number of islands included in this study partitioned into four main categories  
1249 depending on their structure and evolution: 1) '2 X-points' wherein reconnection at two dominant  
1250 X-points forms a magnetic island, 2) '>2 X-points' in which reconnection at two dominant X-  
1251 points forms a magnetic island inside which multiple smaller islands and X-points exist, 3)  
1252 'Coalescence' which describes the merging of two independent magnetic islands during which  
1253 three dominant X-points are reduced to two dominant X-points, and 4) 'Division' which describes  
1254 the process through which one magnetic island is divided into two independent magnetic islands,  
1255 therefore, two dominant X-points become three dominant X-points. The structures are further  
1256 categorized based on their evolution, describing the change in individual magnetic island's

1257 magnetic flux,  $\Delta\psi$ , and area,  $\Delta A$ . The shade of red indicates the relative magnitude of each cell  
 1258 compared to the column's total counts (bottom row), with bright red signifying the largest value.

1259  
 1260 **Table I:** The number of islands included in this study (4786) partitioned into four main categories  
 1261 depending on their structure and evolution.

Quadrants	Structure Categories			
	Category 1 2 X-Points 	Category 2 >2 X-Points 	Category 3 Coalescence 	Category 4 Division 
<b>Q1</b> ( $\Delta A > 0$ & $\Delta\psi < 0$ )	205	40	4	15
<b>Q2</b> ( $\Delta A > 0$ & $\Delta\psi > 0$ )	1716	888	23	72
<b>Q3</b> ( $\Delta A < 0$ & $\Delta\psi < 0$ )	406	46	24	12
<b>Q4</b> ( $\Delta A < 0$ & $\Delta\psi > 0$ )	477	191	15	4
$\Delta A = 0$ or $\Delta\psi = 0$	669	42	0	3
<b>Total</b>	<b>3473</b>	<b>1207</b>	<b>66</b>	<b>106</b>

1262 The four categories include: 1) '2 X-points' wherein reconnection at two dominant X-points forms  
 1263 a magnetic island, 2) '>2 X-points' in which reconnection at two dominant X-points forms a  
 1264 magnetic island inside which multiple smaller islands and X-points exist, 3) 'Coalescence' which  
 1265 describes the merging of two independent magnetic islands during which three dominant X-points  
 1266 are reduced to two dominant X-points, and 4) 'Division' which describes the process through  
 1267 which one magnetic island is divided into two independent magnetic islands, therefore, two  
 1268 dominant X-points become three dominant X-points.

1269 The structures are further divided into based on their evolution, describing the change in individual  
 1270 magnetic island's magnetic flux,  $\Delta\psi$ , and area,  $\Delta A$ .

1271 The shade of red indicates the relative magnitude of each cell compared to the column's total  
 1272 counts (bottom row), with bright red signifying the largest value.

1273  
 1274  
 1275